This file is the final accepted version of the manuscript, published in
https://doi.org/10.1016/j.engstruct.2024.118907

EXPERIMENTAL STUDY ON THE INFLUENCE OF TERRAIN COMPLEXITY ON WIND PRESSURE CHARACTERISTICS OF MID-RISE BUILDINGS

Lee-Sak An[1], Nasrollah Alinejad[2] and Sungmoon Jung[3]*

Abstract

This study investigates the influence of terrain complexity on wind pressure for mid-rise buildings through wind tunnel tests using 50 actual terrain morphologies in the US. A quantitative analysis of the impact of terrain complexity on pressure coefficients at tap lines, area-averaged pressure coefficients, and gust effect factors is conducted by comparing results with homogeneous terrains. A decrease in mean wind speed and an increase in turbulence intensity levels at eave height (50 m) were observed in complex heterogeneous terrains when the effective roughness length was estimated using a conventional anemometric method. Consequently, the magnitude of mean pressure coefficients in homogeneous terrain is typically more conservative than in heterogeneous terrain for all windward walls, roofs, and sidewalls. This trend was observed in both tap lines and area-averaged pressure coefficients. Additionally, it is confirmed that both the gust dynamic pressure factor and the gust response factor tend to increase with roughness length and terrain complexity. For the gust effect factor, both the gust dynamic factor and the gust response factor increase as roughness length increases, resulting in an insignificant change due to roughness length alone. However, the gust effect factor in heterogeneous terrain shows considerable

[1] Postdoctoral Scholar, Department of Civil and Environmental Engineering, FAMU-FSU College of Engineering, 2035 E Paul Dirac Dr, Tallahassee, Florida 32310, United States. Email: lan@eng.famu.fsu.edu

[2] Ph.D. candidate, Department of Civil and Environmental Engineering, FAMU-FSU College of Engineering, 2035 E Paul Dirac Dr, Tallahassee, Florida 32310, United States. Email: na19j@fsu.edu

[3] Professor, Department of Civil and Environmental Engineering, FAMU-FSU College of Engineering, 2035 E Paul Dirac Dr, Tallahassee, Florida 32310, United States. Email: sjung@eng.famu.fsu.edu (corresponding author)

variability, indicating that terrain complexity can amplify the gust effect factor of mid-rise buildings.

Keywords

Wind tunnel testing; Terrain simulator; Terrain complexity; Complex heterogeneous terrain; Mid-rise building; Pressure coefficient; Gust effect factor

1. Introduction

Terrain configuration significantly contributes to uncertainties in wind loads, as emphasized in Davenport's wind loading chain [1]. Terrain roughness, especially impactful for shorter buildings near the ground surface, exposes them to heightened turbulence. In practical applications, engineers often simplify the treatment of terrains with topological complexity by considering them as uniform. Terrains are typically categorized based on an ‘exposure category,’ and this exposure-based approach has gained widespread acceptance [2]. Nevertheless, some studies have suggested that upstream terrain configurations directly impact peak wind loads on building envelopes [3]. The influence of terrain complexity on wind load assessment remains insufficiently explored.

Following Jensen’s wind tunnel experiment, which established the similarity in using a turbulent boundary layer to obtain pressure coefficients in agreement with full-scale values [4], numerous wind tunnel measurements have been conducted to assess wind loads on buildings. The focus has predominantly centered on urban or suburban exposures, emphasizing the impact on building structures. To avoid undersized building models when replicating the entire atmospheric boundary layer (ABL) in a wind tunnel, it is customary to simulate the lower portion commonly known as the atmospheric surface layer (ASL). This approach allows for the use of large-scale building models scaled between 1:25 to 1:100 [5, 6]. The ASL is modelled based on roughness length (z_0)

This file is the final accepted version of the manuscript, published in
https://doi.org/10.1016/j.engstruct.2024.118907

to simulate the underlying surface's influence on turbulent mixing. An effective roughness value for the entire area has been found to be sufficient in areas with moderately homogeneous terrains and smaller-scale inhomogeneity (such as vegetation patches and built structures) [7, 8]. Regarding the concern over lower Reynolds numbers (*Re*) stemming from scaling effects in wind tunnel testing, there is a consensus that *Re* can be relaxed at larger values above a certain threshold (i.e., $Re > 1.0 \times 10^5$) [2].

ASCE 7-22 [2] explicitly defines low-rise buildings as those with a height ratio (the ratio of the mean roof height to the least horizontal plan dimension) smaller than 1. This implies two building classes: low-rise buildings (Height ratio <1) and all other tall buildings with height ratio ≥1. Wang and Kopp [9, 10] additionally classified tall buildings based on aerodynamic considerations, indicating that those with a height ratio>4 can be considered high-rise, with buildings falling between these bounds being classified as mid-rise. Many previous studies have investigated the pressure behaviors of tall building surfaces on boundary-layer flows. Sachs [11] conducted an extensive series of wind pressure measurements in a uniform flow, and these results formed the basis for most modern building codes and standards. Kao [12] found that the impinging turbulent velocity fluctuations were strongly and positively correlated with the fluctuating pressures in the stagnation region on the front face of a rectangular prism. Akins [13] and Akins et al. [14] investigated the mean and fluctuating pressure coefficients on 15 buildings with height ratios ranging from 1 to 8 under the four boundary layers, and their experimental data were used as the aerodynamic basis for the wind loads on tall buildings in ASCE 7. Lin et al. [15] studied the characteristics of wind force on tall buildings with height ratios of 3-5 and plan aspect ratio of 0.33-3.00, confirming that the side wall pressure coefficients became constant as the plan aspect ratio exceeds 2. Kareem [16] represented the experimental measurements and analysis for tall buildings to identify the influence of turbulence on the space-time structure of random pressure field. They observed that increasing turbulence intensity induces early reattachment and associated pressure recovery on the side face. Wang and Kopp investigated the effects of building geometry on tall-building aerodynamic mechanisms for windward walls [17] and separated flow regions [18] based on an experimental database.

Despite extensive studies, the majority of current knowledge is confined to homogeneous (i.e., uniform) terrain, such as roughness length (z_0) of 0.03 m (open) or 0.3 m (suburban). However, real-world terrains have complex morphologies and abrupt roughness changes, and significant knowledge gaps persist regarding the influence of the complex heterogeneous terrain on the pressure experienced by buildings. Only a few studies have discussed the effect of terrain complexity on wind loads. Yu et al. [19] conducted wind tunnel tests using two real city terrain models and proposed a minimum upstream fetch length for wind tunnel testing. Wang and Stathopoulos [3] emphasized the significance of local, small-scale roughness changes in affecting the variation of the wind speed profile above heterogeneous terrain. An et al. [20] conducted extensive wind tunnel testing to explore wind characteristics over complex heterogeneous terrains. They quantified the relationship between the variance of geometric morphology and wind characteristics, ultimately concluding that terrain complexity significantly increased turbulence intensity levels. It is anticipated that statistics of pressure coefficients and reattachment length over complex heterogeneous terrains will differ from those over homogeneous terrains due to the substantial influence of turbulence properties in the approaching wind flow [21, 22]. Moreover, those changes can subsequently influence the area-averaged pressure coefficients and gust effect factors [18].

For the calculation of peak wind loads, the gust effect factor, developed by Solari [23, 24], is currently incorporated into ASCE 7 [2] and the European standard [25]. Quasi-steady theory (QST) is widely employed as the foundational concept for these wind load provisions. QST assumes that pressure fluctuations are a function of the upstream wind speed and provides an approximate solution for pressures at a stagnation point. This can be considered by examining the unsteady Bernoulli equation applied to the stagnation streamline [26]. The flow fields over roofs and around side walls are more complex than the flow near stagnation points on windward walls, with various flow patterns and vortical structures that alter the Gaussian statistics even though QST is reasonably accurate for regions of separated and reattaching flow [27]. The derivation of the gust effect factor for rigid buildings relies on numerous theoretical and parametric assumptions, considering only the effects of non-contemporaneous gust actions over the structures while ignoring the effects of body-generated turbulence. This may lead to deviations in the estimated peak values from the true values [28]. Experimental approaches can compensate for such shortcomings. Therefore, it is of practical importance to investigate the influence of terrain complexity on peak loads using direct measurement data.

This study investigates the impact of complex heterogeneous terrain on wind loads for a typical mid-rise building with a height of 50 m at full-scale. Extensive wind tunnel testing was conducted using real terrain morphologies from 50 sites in the US. To compare pressure results from complex heterogeneous terrains, additional wind tunnel testing was conducted under homogeneous conditions. By comparing the wind pressure coefficients from heterogeneous and homogeneous terrains with similar roughness lengths, the study quantifies the potential errors that may occur when ignoring terrain complexity and assuming a homogeneous terrain. These experimental investigations provide valuable insight into the complex flow fields and the relationships between these flow fields and the surface pressures on the buildings.

This paper is structured as follows: Section 2 details the test setup, covering the wind tunnel, terrain simulator, building model, and the terrain selection process. Section 3 outlines the determination of aerodynamic roughness parameters and exposure categories for selected heterogeneous terrains. Section 4, the wind characteristics are examined by comparing results from heterogeneous terrains with homogeneous terrains. Section 5 presents a comparative analysis of pressure coefficients between homogeneous and complex heterogeneous terrains. Finally, Section 6 provides conclusions.

2. Test Setup and Methodology

In this section, we provided a concise overview of the test setup, including an overview of the facility, the building model, and the site selection process. The DesignSafe-CI repository [29] provides detailed information on the test setup, and Alinejad et al. [30] describes the data collection, validation, and storage procedures on the mentioned repository. For further details on the site selection and the reproduction of heterogeneous terrains from the real sites, refer to An et al. [20] and Alinejad et al. [31].

2.1. Wind Tunnel and Terraformer

Wind tunnel experiments took place at the Natural Hazard Engineering Research Infrastructure (NHERI) facility at the University of Florida [32]. Fig. 1 depicts an open-circuit tunnel with dimensions of 6 m (width) × 3 m (height) × 38 m (length), featuring eight vane axial fans, each powered by a 56-kW electric motor. The flow generated by these fans conditioned by the honeycombs positioned approximately 3 m downwind from the fan bank to reduce fan-generated turbulence and ensure horizontal homogeneity of the velocity profile. This facility accommodates an automated terrain simulator named the "Terraformer." This technology facilitates rapid and precise terrain simulation, addressing the time-consuming and labor-intensive challenges inherent in wind tunnel testing. The Terraformer comprises a configuration of 18 × 62 (totaling 1116 elements) computer-controlled roughness elements arranged in a staggered layout, covering a fetch size of 6 m × 18.6 m. The Terraformer allows for independent height adjustments (0 to 160 mm) of each 100 mm × 50 mm roughness element using an actuator beneath them. LabVIEW software controls the height of each element, and the reconfiguration of all 1116 elements can be accomplished in less than 60 seconds. Thus, the Terraformer effectively replicates diverse upwind terrains. Furthermore, a turntable situated at the end of the upwind fetch allows for the simulation of wind effects on structures at various incidence angles.

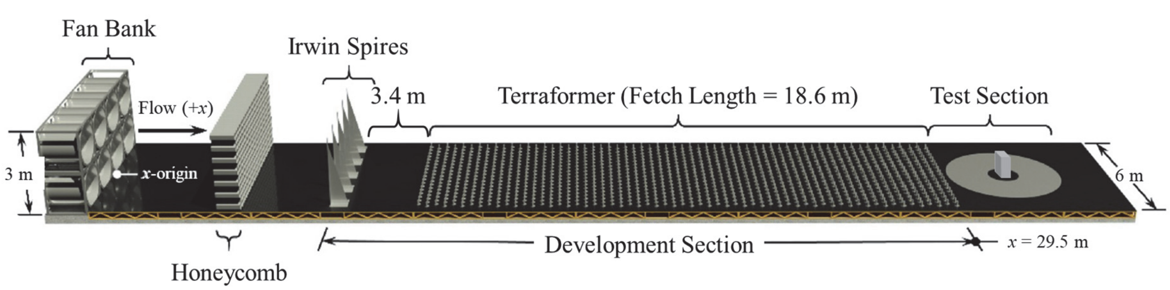

Fig. 1. Schematic plan of the wind tunnel facility at the University of Florida [33].

2.2. Building Model and Measurement Instruments

The building model employed in this study had dimensions of 600 mm (Width) × 300 mm (Length) × 500 mm (Height) in testing scale (60 m (Width) × 30 m (Length) × 50 m (Height) in full-scale) with a flat roof as shown Fig. 2. The building height is taller than 18 m which is the boundary for low-rise building (defined in Chapter 26 in ASCE 7), and the height ratio (about 1.6) is between 1.0 to 4.0. Thus, this building model is categorized as a mid-rise building.

Wind velocity measurements were conducted at a sampling rate of 1250 Hz using three Turbulent Flow Instrumentation Cobra Probes positioned at the midpoint of Terraformer's far end. To obtain the profile, wind speeds were measured at 36 different heights, ranging from 5 mm to 1500 mm above the ground. To minimize adverse scale effects, model length scales in wind tunnel testing are typically within the range of 1:10 to 1:100 [34]. We adopted a 1:100 scale, meaning the maximum vertical measurement height of 1500 mm in test scale corresponds to 150 m in full-scale representation. The speed scale is 3.5 ($\frac{V_{full}}{V_{test}} = \frac{35\ m/s}{10\ m/s}$), where V_{full} represents approximate hurricane conditions at full scale [35], and V_{test} represents the wind speed in the wind tunnel at a full-scale height of 10 m. Since the minimum test duration required to achieve an equivalent 10-minutes full-scale measurement is 42 seconds, wind speed measurements in this experiment were taken over a period of 45 seconds.

Pressure measurements were collected using eight high-speed electronic scanning modules from Scanivalve ZOC33 [36]. The pressure taps were connected to the modules via 122 cm long urethane tubing, and the sampling frequency was set at 625 Hz. Tubing effects on pressure measurements were adjusted [37], to minimize the distortion on amplitude and phase shift. The building model was outfitted with a total of 216 pressure taps, comprising 102 roof taps and 114 wall taps. Fig. 2 provides a visual representation of the building model and target tap lines that will be investigated. Tap lines will be selectively used to examine the main pressure behavior at each incident wind angle. The tap lines in Fig. 2 (a) and (b) run parallel and perpendicular to the long building dimensions and are used to examine the pressure behavior for 0° and 90° wind angles,

This file is the final accepted version of the manuscript, published in
https://doi.org/10.1016/j.engstruct.2024.118907

respectively. Fig. 2 (c) is used to examine changes in wind pressure behavior in the horizontal direction on the windward and side walls. Each line are further classified into (1)~(3) depending on the region. Line number and surface number are used to refer to the target area. For example, the (1) of Line 1 is indicated as Line 1-(1).

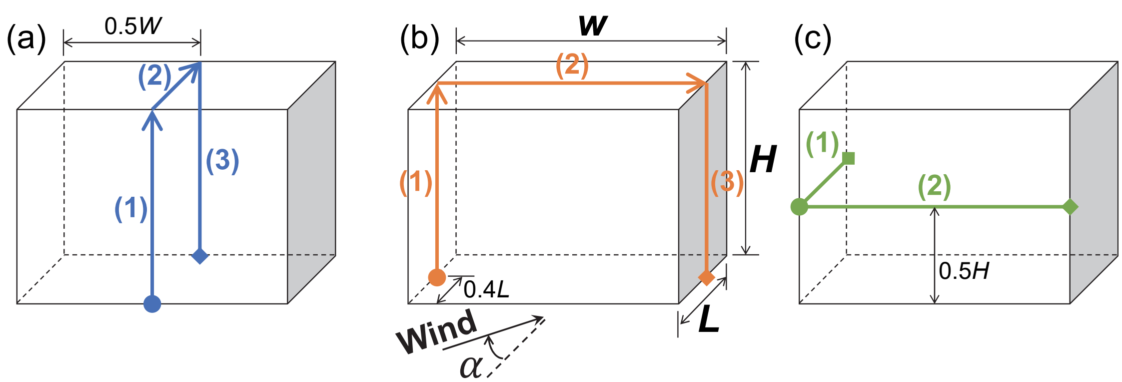

Fig. 2. Layout of pressure tap lines on the building model: (a) Line 1; (b) Line 2; and (c) Line 3.

2.3. Selection of Heterogeneous Terrains

Complex heterogeneous terrain configurations sourced from real terrains were compiled for wind tunnel testing. The primary data source was the National Land Cover Database (NLCD) [38] provided by the US Geological Survey. A total of 529 sites from 32 US states prone to hurricanes were selected. Each site image obtained from the NLCD dataset had dimensions of 3840 m × 3840 m. To create more comprehensive cases, each image was divided into four smaller images facing north, south, west, and east, with dimensions of 1860 m × 540 m each as shown in Fig. 3. This division resulted in a total of 2116 images for analysis.

This file is the final accepted version of the manuscript, published in
https://doi.org/10.1016/j.engstruct.2024.118907

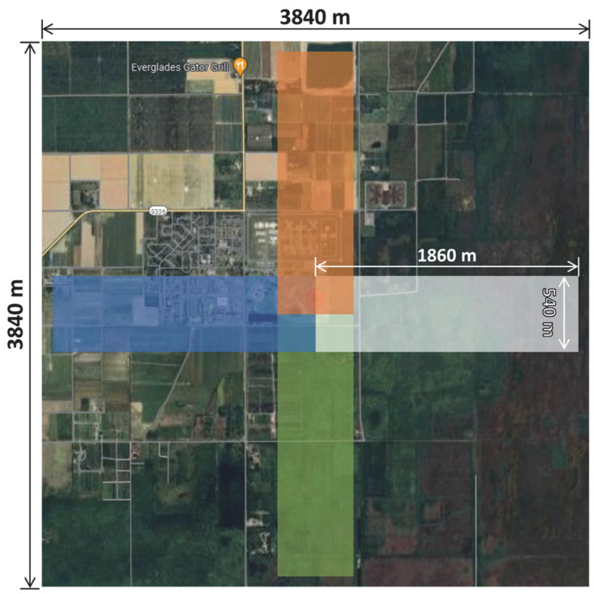

Fig. 3. Visual explanation of how one NLCD dataset was separated into four directions at Site ID 1 (Miami Florida, [Latitude, Longitude] = [25.41191, -80.4964]). Google map was used instead of NLCD for high-resolution visualization.

The NLCD dataset furnished land coverage information for each pixel of the image, with a resolution of 30 m (each pixel covering 30 m × 30 m of land). By utilizing specific land coverage types and their corresponding local roughness length z_0^{local} values, as shown in Table 1, each pixel in the image was assigned an appropriate z_0^{local} value. Therefore, an image containing an area of 1860 m × 540 m has z_0^{local} information of 62 × 18 = 1116.

Table 1. Land coverage classification in NLCD images (z_0 range is based on Wieringa [8], Wang and Stathopoulos [3], Davenport [39], Vihma and Savijärvi [40], and He et al. [41])

Land cover	**z_0^{local} (full-scale, m)**	**Block height (test-scale, m)**
Open Water, Perennial Ice, Snow	0.0003	0.0050
Woody Wetlands, Emergent Herbaceous Wetland	0.0025	0.0085
Barren Land	0.0055	0.0105
Dwarf Scrub, Shrub Scrub	0.0105	0.0125
Pasture, Hay	0.0155	0.0145
Grassland, Herbaceous, Cultivated Corps	0.0205	0.0155
Low-rise building	0.5	0.0545
Mid- to high-rise	1	0.0770
Deciduous Forest, Evergreen Forest, Mixed Forest	1.65	0.1000

To select representative terrains among 2116 sites with distinct stochastic properties of z_0^{local}, the k-means algorithm [42]—a commonly used clustering technique minimizing the average

This file is the final accepted version of the manuscript, published in
https://doi.org/10.1016/j.engstruct.2024.118907

squared distance between points within the same cluster—was applied in the 2D space defined by the mean $\mu(z_0^{local})$ and standard deviation $\sigma(z_0^{local})$ as illustrated in Fig. 4. $\mu(z_0^{local})$ and $\sigma(z_0^{local})$ can be calculated from the 1116 z_0^{local} information of each image. Thus, each dot in Fig. 4 indicates a site among 2116 sites, and each color represents 50 distinct clusters obtained through the k-means algorithm. Then, the cluster centroids were identified as 50 representative sites. More details on this process are kindly introduced in previous studies [20, 31].

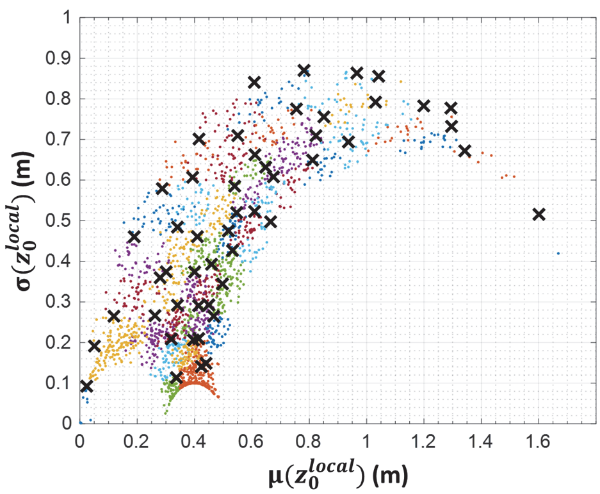

Fig. 4. The clustering results using $\mu(z_0^{local})$ and $\sigma(z_0^{local})$ for 2116 sites. Dots represent the investigated sites, and cross marks indicate the selected 50 sites. (Reproducing from An et al. [20])

In the wind tunnel, the z_0^{local} values were correlated with the corresponding block heights using the method fully described by Alinejad et al. [31]. Fig. 5 provides examples of the selected sites and their corresponding block height maps in the Terraformer, along with the simulated terrain morphology generated for sites (i) 13; (j) 21; and (k) 29. Even though NLCD also provided aerial photos, the resolution was very low. Thus, the images of the locations from Google Maps are re-captured and shown in Fig. 5 (a). As shown in Fig. 5 (b), each complex heterogeneous terrain contains 1116 block heights, which is corresponding the z_0^{local}.

An et al. [20] used the coefficient of variation of logarithmic z_0^{local} ($\mathrm{COV}_{\ln(z_0)} = \sigma(\ln(z_0^{local}))/\mu(\ln(z_0^{local}))$) as a measure of the terrain complexity of each complex heterogeneous terrain. They took the logarithmic due to the wide distribution of z_0 values spanning multiple orders of magnitude and the substantial impact of ln (z_0) on wind speed according to the logarithmic wind law. Thus, $\mathrm{COV}_{\ln(z_0)}$ was used as the parameter when checking the influence of terrain complexity on the wind pressure on the mid-rise buildings.

This file is the final accepted version of the manuscript, published in
https://doi.org/10.1016/j.engstruct.2024.118907

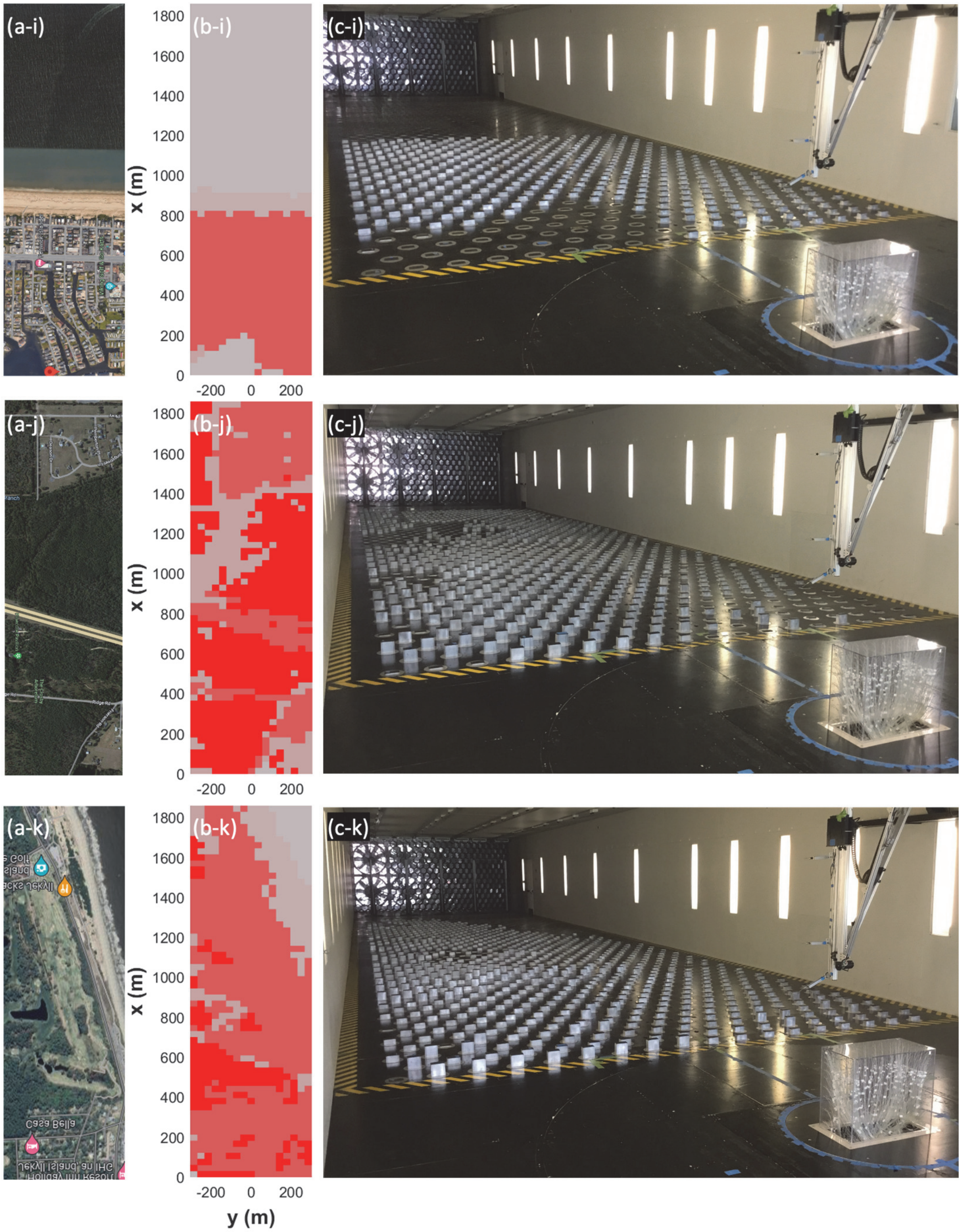

Fig. 5. Example of complex heterogeneous terrains: (a) Aerial view (corresponding Google Map instead of NLCD image was used for better visualization); (b) Block height map; and (c) Actual photo in the wind tunnel with (i) site 13; (j) site 21; and (k) site 29.

2.4. Summary of Parameters for Wind Load

In this subsection, we summarize the pressure coefficient and the gust effect factor derived directly from the measured data in the time domain. Following the usual convention in wind engineering, the pressure coefficient at a specific point of interest, denoted as C_P^i, is defined as the ratio of the measured building surface gauge pressure to the dynamic pressure at roof height, expressed in Eq. (1):

$$C_P^i(t) = \frac{P^i(t)}{0.5\rho\bar{u}^2} \tag{1}$$

Here, $\bar{u}$ represents the mean wind speed at the roof height (50 m), and ρ denotes air density. $P^i(t)$ indicates the measured net wind pressure at the *i*-th tap, signifying the value obtained by subtracting the reference pressure from the gauge-measured wind pressure. Internal reactions are not considered, following St. Pierre et al. [43].

For wind loads, particular interest lies in the area-averaged pressure, integrating the pressures on each wall simultaneously. The area-averaged pressure P can be determined using the tributary area for each tap, as expressed in Eq. (2):

$$P(t) = \sum_{i=1}^{N} P^i(t)\frac{A_i}{A} \tag{2}$$

Where A_i is the tributary area of the *i*-th tap, A is the total surface area. The tributary area of a tap was determined based on halving the distance between that tap and adjacent taps. Note that, due to the non-uniform spacing of taps, these tributary areas are not uniform.

Gustiness in wind introduces dynamic loading effects on the structural system, which can be assessed in terms of a gust effect factor *G*. To evaluate the peak response of the system, the peak wind load must be considered. For estimating wind load, the peak pressure $\hat{P}$ and the peak dynamic pressure $\hat{q}$ are utilized with the gust effect factor *G* as follows:

$$\hat{P} = G\hat{q}\overline{C_P} \tag{3}$$

The gust effect factor can be estimated using Eq. (4) directly from the measured data in the time domain. The peak pressures were estimated using the Lieblein BLUE method [44], involving dividing time series data into 16 equal segments, obtaining 16 maxima for each, and taking the mean values of the Gumbel distribution as the estimated peak values. No pressure filters were applied, allowing all coefficients to be considered instantaneous. By rearranging Eq. (3), G can be expressed as follows:

$$G = \frac{\hat{P}}{\hat{q}\overline{C_P}} = \frac{\hat{P}}{\overline{P}} \times \frac{\bar{u}^2}{\hat{u}^2} = \frac{G_P}{G_u^2} \tag{4}$$

Here, $\bar{P}$ and $\hat{u}$ are the mean pressure and the peak wind speed at the roof height, respectively. $G_P(= \hat{P}/\bar{P})$ and $G_u(= \hat{u}/\bar{u})$ indicate the gust response factor and gust dynamic pressure factor. The peak wind speed $\hat{u}$ can be determined as the 3-s gust wind speed, representing the peak wind speed measured with a 3-s moving averaged wind speed data. Also, since the testing period is 45 seconds, equivalent to approximately 20 minutes (1200 seconds) in full-scale, the measured mean wind speed $\bar{u}$ was transformed into hourly mean wind speeds based on Fig. C26.5-1 in ASCE 7, known as the Durst curve [45], i.e., $V_{1200}/V_{3600} = 1.05$.

3. Exposure Categorization

The concept of exposure categories is widely integrated into design standards globally, including the US [2], Canada [46], and Europe [47], to streamline the design process. In the US, ASCE 7-22 classifies terrain into one of three exposure categories: B to D. Each category has a range of the roughness length (z_0), serving as a representative measure of the aerodynamic characteristics of the terrain, as outlined in Table 2 [2]. Exposure A was omitted in ASCE 7-02 due to the substantial variability of wind in this terrain, arising from local channeling and wake-buffeting effects. For this reason, this study disregarded cases identified as exposure A.

Table 2. Range of z_0 by exposure category [2] (adopted from ASCE 7-22 Table C26.7-1).

Exposure category	**Lower limit of z_0 (m)**	**Typical value of z_0 (m)**	**Upper limit of z_0 (m)**
A[a]	0.7	2	-
B[b]	0.15	0.3	0.7
C[c]	0.01	0.02	0.15
D[d]	-	0.005	0.01

[a]Centers of large cities (eliminated since ASCE 7-02)
[b]Urban and suburban terrain
[c]Open terrain
[d]Flat, unobstructed area and water surfaces

To determine the exposure category of each complex heterogeneous terrain, the effective roughness length ($z_{0,\mathrm{eff}}$) was obtained through an anemometric approach [48, 49]. For the anemometric approach, curve fitting techniques are employed to align the log law [50] with velocity profile measurements, as shown in Eq. (5). The log law is widely acknowledged for its accuracy in representing the theoretical mean wind speed within the lower portion of the ABL [51].

$$U(z) = \frac{u_*}{\kappa} \ln\left(\frac{z-d}{z_0}\right) \tag{5}$$

$U(z)$ represents the mean along-wind speed at height z, and κ is von Karman's constant (=0.40). This equation holds when the surface is aerodynamically fully-rough, meaning that the surface-roughness Reynolds number $Re_* = u_* z_0/\nu > 2.5$ [52], where ν is the kinematic viscosity of air. All wind tunnel testing results in this study exhibited Re_* values larger than 2.5. Since wind profiles in the ASL are crucial for designing buildings [53], we estimated aerodynamic roughness parameters (ARP), including friction velocity (u_*), zero-displacement height (d), and z_0, within inertial sublayer (ISL) [49]. The ISL nominally exists between $z_w < z < 0.25\delta$, where z_w is a wake diffusion height, turbulent mixing sufficiently blends individual element wakes to produce laterally homogeneous flow, and δ is a gradient height. z_w was assumed to be $1.9H$ [54], where H is the average height of the block elements in 2/3 of the width direction (x-axis) × 1/6 of the length direction (y-axis) (12 lines × 11 lines = 132 block elements) in front of measurement points. δ can be determined by using quadratic function fitting. The outer layer of the wind profile, which is approximately parabolic in shape, is fitted by the quadratic function as described by Guo [55]. Then, the value δ is found by setting $\partial U/\partial z = 0$. It is noteworthy that the anemometric method must be distinguished from the morphologic method. The anemometric method uses wind profile measurements, while the morphologic method uses the terrain morphologic information to determine the $z_{0,\mathrm{eff}}$.

Fig. 6 showcases the semi-logarithmic profiles of measured and predicted mean wind speed at sites 8 and 42. The profiles are presented in the dimensionless form U/u^* and $(z-d)/z_0$ so that the slope of the fits equals to $1/\kappa$ (i.e., 2.5). ARP estimates obtained from the anemometric approach are utilized to plot the predicted wind profiles. The predicted wind profile aligns well with the measured wind profiles within the ISL range, indicating that $z_{0,\mathrm{eff}}$ based on the anemometric approach accurately represents the wind profiles of the corresponding complex heterogeneous terrains.

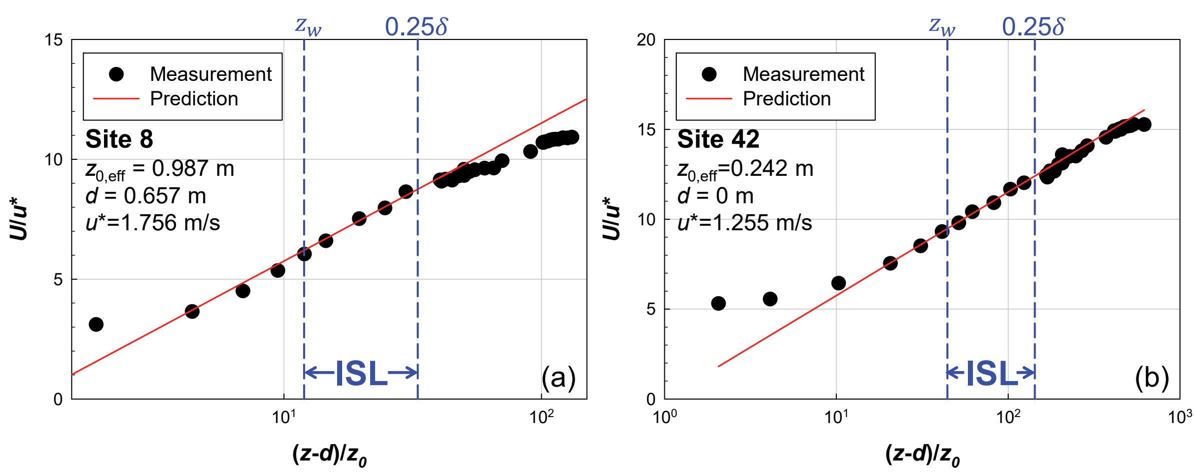

Fig. 6. Examples of the ARP calibration based on anemometric approach: (a) Site 8; and (b) Site 42.

Table A 1 in Appendix A presents the calculated $z_{0,\text{eff}}$ values along with their corresponding exposure categories for heterogeneous terrains. Exposure B contains the highest number of sites (34 of 50 sites), as expected, given that exposure B encompasses a relatively wider range of z_0 values compared to exposure C and D, making it the most common exposure category. Additionally, as reference cases for comparison with the complex heterogeneous terrains, preliminary wind tunnel testing was conducted for homogeneous terrains. All block heights in the Terraformer were uniformly changed to achieve a various range of $z_{0,\text{eff}}$, as shown in Table A 2.

4. Wind Characteristics

Along the wind load chain, the terrain affects the wind profile approaching the structure. Therefore, it is essential to examine changes in wind characteristics due to heterogeneous terrain compared to homogeneous terrains. The ARPs were calibrated using the ISL, particularly in the relatively lower regions. Therefore, even though some homogeneous and complex heterogeneous terrains show a similar $z_{0,\text{eff}}$ level, the wind characteristics can differ at higher height. Fig. 7 shows (a) normalized mean wind speed $U(z)/U_{max}$ and (b) turbulence intensity $I_u(z)$ with varying $z_{0,\text{eff}}$ at two heights: (i) 10 m and (j) 50 m (i.e., roof height). For homogeneous terrain, unlike the test measuring wind pressure shown in Table A 2, the test measuring only the wind profile while varying block height was performed on more cases. Consequently, the number of data points for homogeneous terrain is much richer than in Table A 2. For complex heterogeneous terrain, exposure B and C were plotted separately for visibility, while the identical marker was used for the homogeneous cases since it is a reference. Each marker represents a result obtained from an experiment at one site. Thus, for heterogeneous terrains, exposure B and C contain 34 and 12 scatters, respectively. As $z_{0,\text{eff}}$ increases, $U(z)/U_{max}$ decreases, and $I_u(z)$ increases at both 10 m and

50 m heights. However, relatively lower $U(z)/U_{max}$ and higher $I_u(z)$ are observed in heterogeneous terrain. This is consistent for both 10 m and 50 m heights. The greater energy dispersions due to terrain complexity on heterogeneous terrains may result in lower mean wind speeds and higher turbulence intensity compared to homogeneous terrain even though $z_{0,\mathrm{eff}}$ was calculated similarly.

The quantitative difference in wind profiles with similar roughness lengths is further illustrated in Fig. 8. It displays the ratio of (a) mean wind speed (U(50 m)/U(10 m)) and (b) turbulence intensity (I_u(50 m)/I_u(10 m)) measured over both complex heterogeneous and homogeneous terrains. It should be noted that wind tunnel testing on homogeneous terrain was performed for a wide variety of block heights to identify wind speed characteristics, but the test cases in which pressure was measured in the mid-rise building were limited, as shown in Table A 2.

Additionally, U(50 m)/U(10 m) and I_u(50 m)/I_u(10 m) from the field measurement data of Engineering Sciences Data Unit (ESDU) [56, 57] is presented for comparison in Fig. 8. U(50 m)/U(10 m) from ESDU is relative with testing results, but I_u(50 m)/I_u(10 m) shows some discrepancies. Considering that complex heterogeneous terrain is a more realistic case than homogeneous terrain, it is a reasonable result that I_u(50 m)/I_u(10 m) of heterogeneous terrain is mainly distributed between the result of homogeneous terrain and ESDU. However, as $z_{0,\mathrm{eff}}$ increases and the terrain becomes increasingly rough, the difference between homogeneous terrains and complex heterogeneous terrains almost disappears. This is consistent with the results in previous study [20]. They observed that the difference between heterogeneous and homogeneous terrains is significant for lower $z_{0,\mathrm{eff}}$ values, indicating relatively smooth terrains. In these cases, the influence of terrain complexity on wind characteristics becomes more prominent. As $z_{0,\mathrm{eff}}$ increases, a general trend of decreasing difference can be observed. If the terrain itself is already rough enough, terrain complexity has little effect on wind characteristics.

This file is the final accepted version of the manuscript, published in
https://doi.org/10.1016/j.engstruct.2024.118907

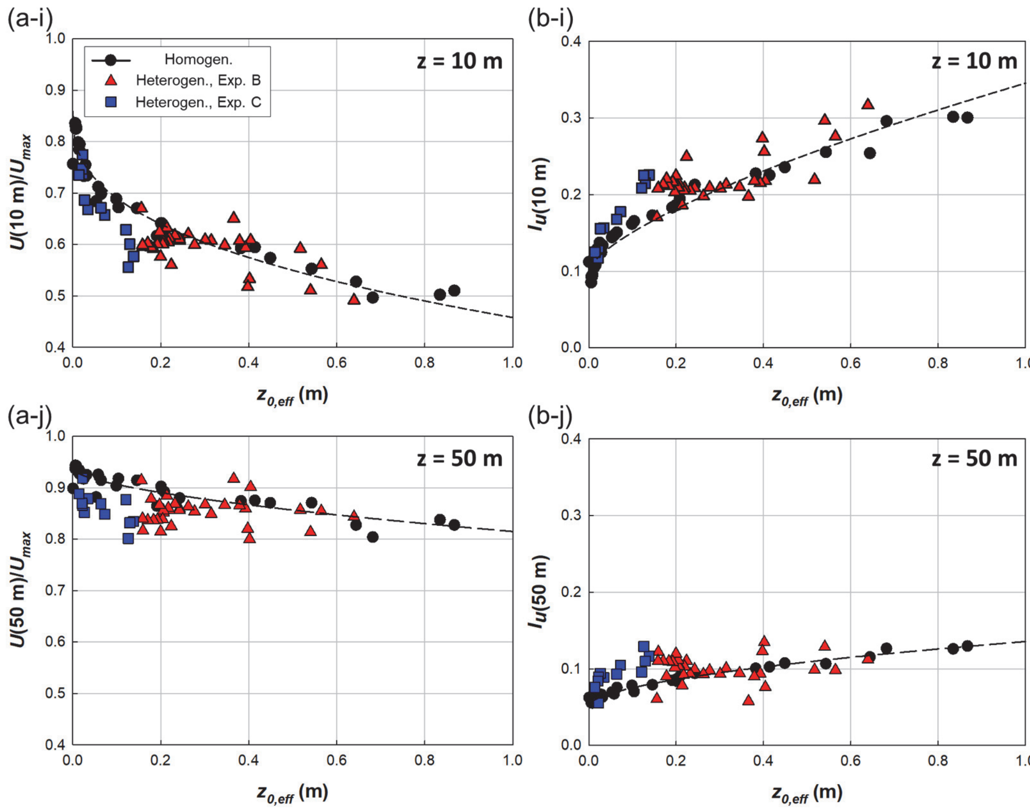

Fig. 7. Comparison of wind characteristics over homogeneous and heterogeneous terrains: (a) Mean wind speed; and (b) Turbulence intensity at (i) 10 m; and (j) 50 m heights.

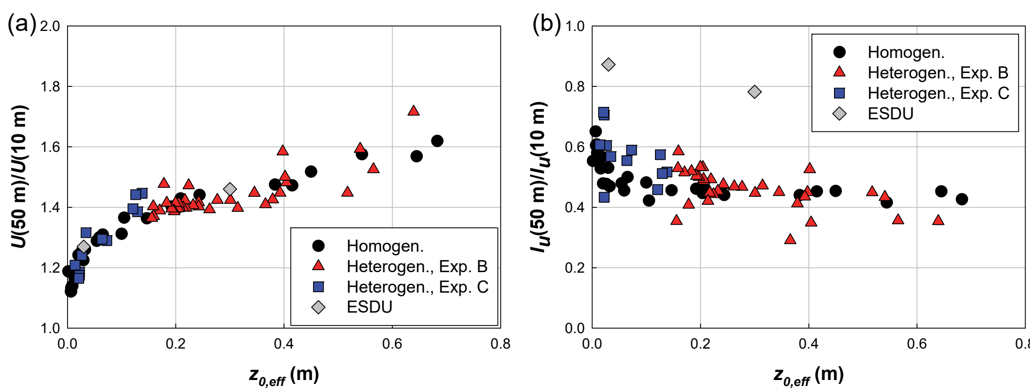

Fig. 8. Ratio of wind characteristics between 10 m to 50 m heights: (a) Mean wind speed; and (b) Turbulence intensity.

Ensuring feasibility in the turbulence property of the inflow wind is crucial for estimating and comparing unsteady wind loads. Fig. 9 presents the wind power spectrum at 10 m and 50 m (eave

This file is the final accepted version of the manuscript, published in
https://doi.org/10.1016/j.engstruct.2024.118907

height) for both complex heterogeneous and homogeneous terrains, featuring similar $z_{0,\mathrm{eff}}$ values (≈0.2 m). The power spectrum was calculated using the Fast Fourier Transform (FFT) and the Welch method [58]. The complete full-scale time series were divided into 1-minute sub-segments with a 50% overlap. To reduce side-lobe leakage, a Hamming window was employed. Moreover, the plots include the empirical model from ESDU [59], as defined by Eq. (6), for comparison.

$$\frac{nS_{uu}}{\sigma_u^2} = \frac{4f}{(1 + 70.8f^2)^{5/6}} \tag{6}$$

Here, S_{uu} signifies the power spectrum for the longitudinal turbulence component, n is the frequency (Hz), σ_u represents the standard deviation of the fluctuating wind components, and $f = nL_u^x/U$, where L_u^x stands for the longitudinal integral length scale, and U is the mean wind speed.

For both heights and types of terrain, the measured spectrum demonstrates good agreement with the ESDU empirical model. Since the wind flow at lower heights is strongly influenced by surface roughness, there is a slight difference between the measurements at 10 m height and ESDU data, while the spectra at 50 m are more similar to ESDU. At a height of 50 m, the homogeneous site contains more energy at higher frequencies compared to the heterogeneous case, and the measured power spectrum over heterogeneous terrain is closer to ESDU. Heterogeneous terrain may induce more shear and mixing in the boundary layer, which aligns well with the assumptions made in the ESDU model. However, both terrains follow Kolmogorov's -5/3 law well at a height of 50 m and simulate the inertial subrange of turbulent flow well.

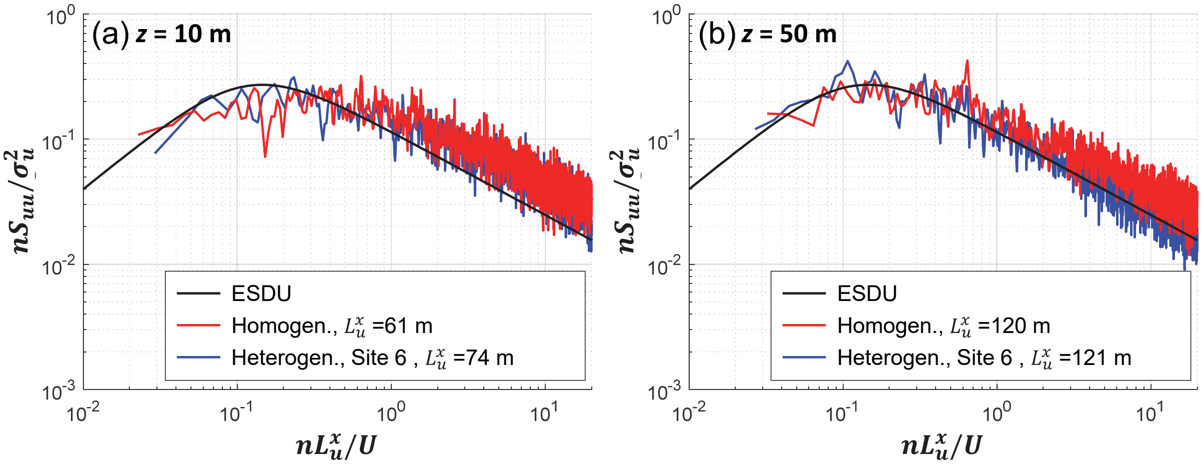

Fig. 9. Wind power spectrum for homogeneous terrain and complex heterogeneous terrain: (a) z=10 m; (b) z=50 m (roof height).

5. Results and Discussion

5.1. Pressure Coefficient along Tap Lines

Fig. 10 illustrates the (i) mean ($\overline{C_P}$), (j) root mean square ($\widetilde{C_P}$), (k) maximum ($\widehat{C_P}$), and (l) minimum ($\breve{C_P}$) pressure coefficients at the target tap lines over exposure B. Selected wind angles that showed significant results were presented for each tap line. For Line 1 and 2, the incident wind angle is (a) 0° and (b) 90°, respectively. For Line 3, the results for two wind angles are presented: (c) 0° and (d) 90°. The statistics derived from complex heterogeneous terrains are presented as boxplots. The line inside each box represents the median of the pressure coefficient statistics. The top and bottom edges of each box denote the upper and lower quartiles (the 0.75 and 0.25 quantiles, respectively). The distance between these edges is the interquartile range (IQR). The whiskers extend to the non-outlier minimum and maximum values, which are the lowest and highest data points that are not considered outliers. Outliers are defined as values that lie more than 1.5×IQR away from either the top or bottom of the box. For comparison, the results from homogeneous cases within exposure B ($z_{0,\text{eff}}$ of 0.2 m and 0.7 m) are presented as lines.

As shown in Fig. 10 (i), the $\overline{C_P}$ in all tap lines does not vary much within exposure B. In detail, not only is there little difference between homogeneous terrain and complex heterogeneous terrain, but there is no significant change within heterogeneous cases, i.e., the boxplots are distributed in narrow ranges. Similar results were also observed in Wu and Kopp [60] and Wang and Kopp [9]. It is worth mentioning that the mean pressure coefficient does not vary with terrain in ASCE 7, such that terrain is assumed to only affect the gust wind speeds but not the building aerodynamics.

Also, the statistics with a $z_{0,\text{eff}}$ of 0.7 m in the homogeneous terrain (red line) show similar results to the upper bound in the magnitude of the heterogeneous terrain. Given that 0.7 m of $z_{0,\text{eff}}$ corresponds to the upper boundary in exposure B (See Table 2), terrain complexity over heterogeneous terrains does not add significant variability to statistics of C_P when having similar $z_{0,\text{eff}}$. Based on these observations, it can be suggested that the change in $\overline{C_P}$ within the same exposure category can be ignored even though the roughness length or terrain complexity has been changed.

When comparing Line 1-(1) in Fig. 10 (a-i) and Line 2-(1) in Fig. 10 (b-i), no significant difference was observed in the maximum magnitude of $\overline{C_P}$ on the windward wall between 0° and 90° of the incident wind angles. Similarly, the level of pressure coefficient at the windward wall in the lateral direction is also similar at any wind angle as shown in Line 3-(2) in Fig. 10 (c) and Line 3-(1) in Fig. 10 (d). This consistency was also observed in previous studies [13, 14].

The roof and side wall also show similar trend. The minimum $\overline{C_P}$ on the roof are about -1.0 for both Line 1-(2) and Line 2-(2). In the case of side wall, the minimum $\overline{C_P}$ was about -0.8 for both

This file is the final accepted version of the manuscript, published in
https://doi.org/10.1016/j.engstruct.2024.118907

Line 3-(1) of 0° and Line 3-(2) of 90°. It suggests that positive pressures on the windward wall and the suction on the roof around leading-edge are not strongly dependent on the dimension of the mid-building in this study.

However, the minimum magnitude of $\overline{C_P}$ in the flow-separated regions can change depending on the along-wind dimension of the building because the pressures on the longer sides are less negative due to flow reattachment and a more complete pressure recovery. For instance, Line 1-(2) in Fig. 10 (a-i) shows the $\overline{C_P}$ of approximately -0.6 was observed at the downwind edge, while Line 2-(2) in Fig. 10 (b-i) shows the $\overline{C_P}$ decreased to almost 0. In the case of side wall, comparing Line 3-(2) when the incident wind angle is 0° (Fig. 10 (c-i)) and Line 3-(1) when the wind angle is 90° (Fig. 10 (d-i)), the former maintains about -0.8 of $\overline{C_P}$, but in the latter, the magnitude of $\overline{C_P}$ decreases to close to 0.

In contrast to $\overline{C_P}$, as depicted in Fig. 10 (j) to (l), $\widetilde{C_P}$, $\widehat{C_P}$, and $\breve{C_P}$ exhibit more pronounced variance than $\overline{C_P}$ with changes in $z_{0,\mathrm{eff}}$. However, there is still no significant difference observed in the range of statistics between homogeneous terrain and complex heterogeneous terrain. The red line closely aligns with the upper bound of the magnitude of $\widetilde{C_P}$, $\widehat{C_P}$, and $\breve{C_P}$ as well. Terrain complexity does not exert a significant effect on the variance of pressure coefficients on the mid-rise building.

Fig. 11 illustrates (i) the peak $\overline{C_P}$ and (j) the maximum $\widetilde{C_P}$ on the tap lines for (a) windward wall, (b) roof, and (c) side wall, with an incident wind angle of 90°. The black dashes in Fig. 11 (i) and (j) represent the average peak $\overline{C_P}$ and the regression results of maximum $\widetilde{C_P}$ over the homogeneous terrains, respectively. As previously discussed in Fig. 10, $\overline{C_P}$ does not vary significantly with changes in $z_{0,\mathrm{eff}}$, and this trend is observed in Fig. 11 (i).

The average peak $\overline{C_P}$ for the windward wall, roof, and sidewall is 1.04, -1.01, and -0.88, respectively. In heterogeneous terrain, these values are distributed between 0.83 and 0.94, -0.86 and -1.05, and -0.75 and -0.90, indicating a potential decrease of 15-20% due to terrain complexity. It is evident that the peak $\overline{C_P}$ from the homogeneous terrain exhibits a larger magnitude than that from heterogeneous terrains, approaching the upper bound of the complex heterogeneous terrain. This is because the mean wind speed is lower in complex heterogeneous terrain when $z_{0,\mathrm{eff}}$ is similar.

On the other hands, the magnitude of the maximum $\widetilde{C_P}$ increases with the rise of $z_{0,\mathrm{eff}}$ for both homogeneous and complex heterogeneous terrains on all surfaces. Additionally, terrain complexity amplifies the fluctuations of the maximum $\widetilde{C_P}$. For instance, with $z_{0,\mathrm{eff}}$ around 0.2 m on the windward wall, $\widetilde{C_P}$ fluctuates between approximately 0.16 and 0.27 for heterogeneous terrain, while it remains around 0.24 for homogeneous terrain. Similarly, on the roof, the maximum $\widetilde{C_P}$ ranges from 0.17 to 0.27 in heterogeneous terrains compared to 0.25 in homogeneous terrain. This suggests a potential difference of about -10~30% attributable to terrain complexity for the maximum $\widetilde{C_P}$.

This file is the final accepted version of the manuscript, published in https://doi.org/10.1016/j.engstruct.2024.118907

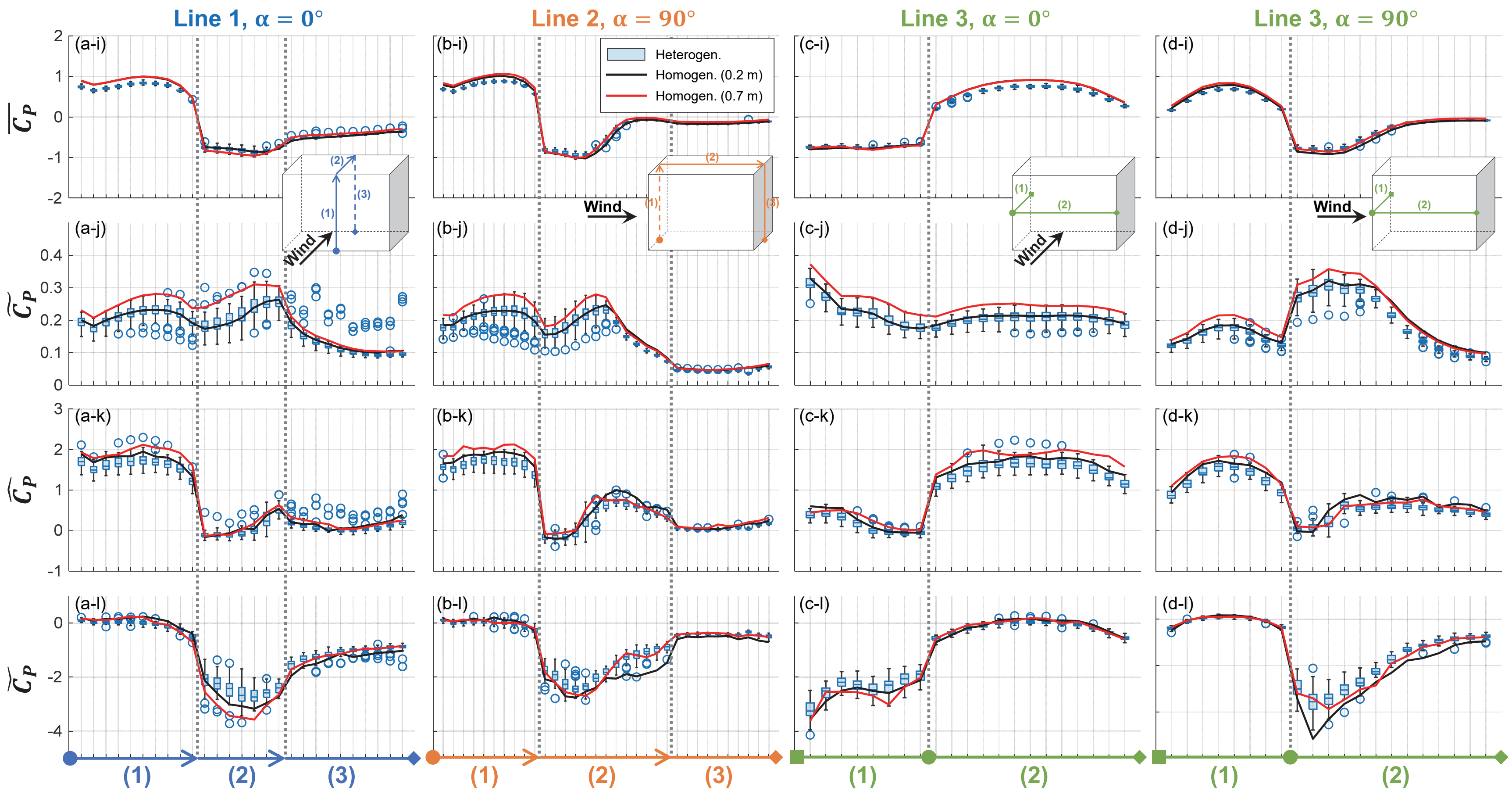

452

453 Fig. 10. Statistics of pressure coefficient for Exposure B: (a) Line 1 at wind incident angle of 0°; (b) Line 2 at wind incident angle of 90°; (c) Line 3 at wind
454 incident angle of 0°; and (d) Line 3 at wind incident angle of 90° with (i) mean ($\overline{C_P}$); (j) root mean square ($\widetilde{C_P}$); (k) maximum ($\widehat{C_P}$); and (l) minimum ($\widecheck{C_P}$)
455 pressure coefficients.

456

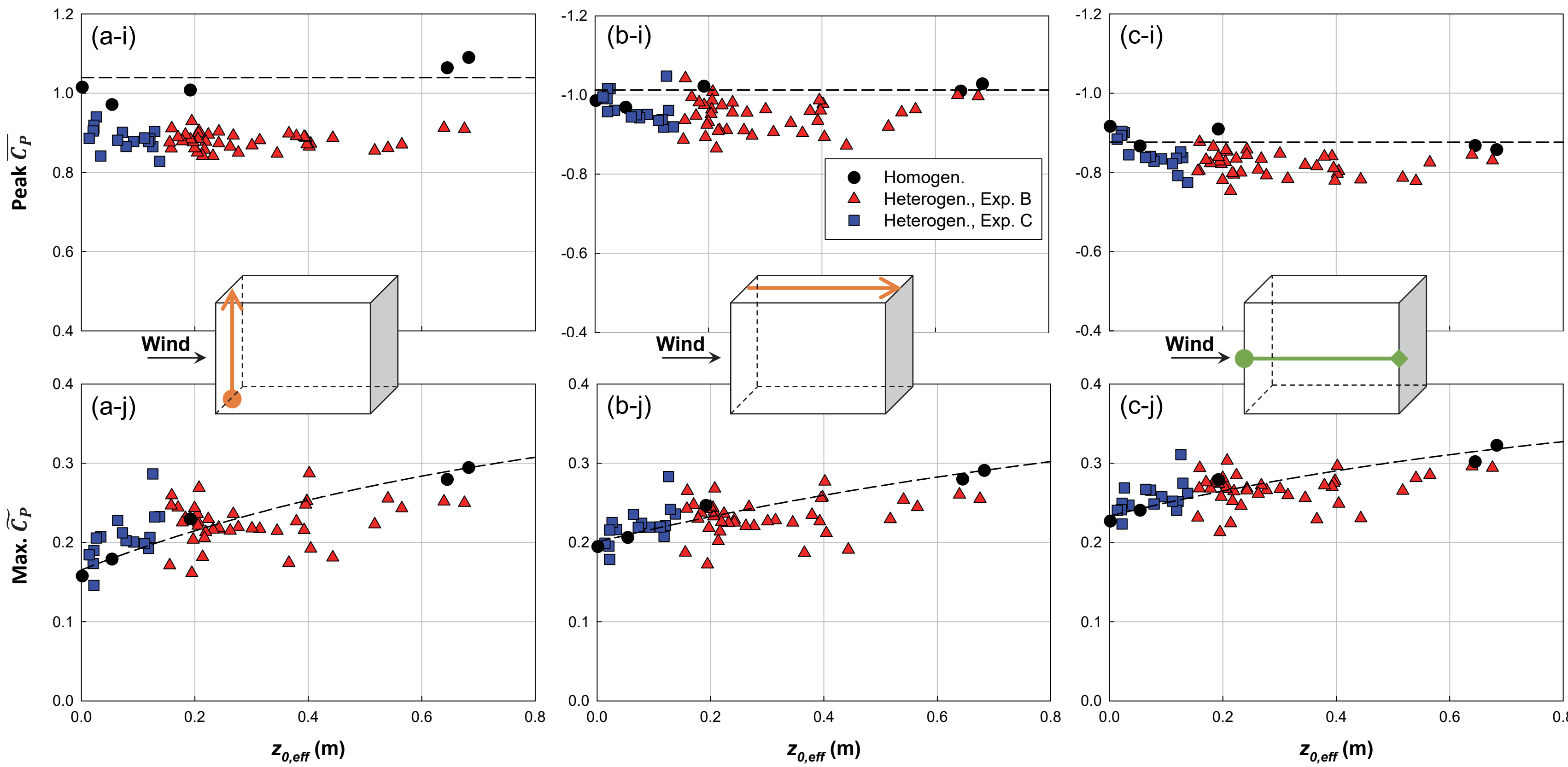

Fig. 11. Comparison of peak wind pressures over homogeneous and heterogeneous terrains at a wind incident angle of 90°: (a) Windward wall (Line 2-(1)); (b) Roof (Line 2-(2)); and (c) Side wall (Line 4-(1)): with (i) Peak $\overline{C_P}$ and ;(j) Maximum $\widetilde{C_P}$. Peak $\overline{C_P}$ means maximum $\overline{C_P}$ for windward wall and minimum $\overline{C_P}$ for roof and side wall.

5.2. Area-Averaged Pressure Coefficient

Fig. 12 illustrates (i) area-averaged $\overline{C_P}$ and (j) area-averaged $\widetilde{C_P}$ with varying $z_{0,\mathrm{eff}}$ for (a) windward wall, (b) roof, and (c) side wall, with an incident wind angle of 90°. Note that the area-averaged pressure integrates the pressures on each wall simultaneously. Black dash presents the average of the area-averaged $\overline{C_P}$ and the regression results of the area-averaged $\widetilde{C_P}$ over the homogeneous terrains, respectively.

The averaged value of the area-averaged $\overline{C_P}$ for homogeneous cases is 0.76, -0.49, and -0.45 for the windward wall, roof, and side wall, respectively. The results from heterogeneous terrains are distributed between 0.60~0.72, -0.41~-0.54, and -0.38~-0.55 for windward wall, roof, and side wall, respectively. Similar to the peak $\overline{C_P}$ on the tap lines, the results from homogeneous terrains are close to the upper bound of the area-averaged $\overline{C_P}$. The magnitude of the area-averaged $\overline{C_P}$ in heterogeneous terrains can decrease up to 20% compared to that in homogeneous terrains. The cause of these results is expected to be the low mean wind speed in complex heterogeneous terrain.

For area-averaged $\widetilde{C_P}$, similar to the maximum $\widetilde{C_P}$ on the tap lines, the result from heterogeneous terrains shows significant variability. When $z_{0,\mathrm{eff}}$ is about 0.2 m on windward wall, the area-averaged $\widetilde{C_P}$ was approximately 0.15 for homogeneous terrain, while those of 0.11 to 0.18 were observed for heterogeneous terrain. The area-averaged $\widetilde{C_P}$ can increase up to 20% due to the terrain complexity.

Through these observations, it can be concluded that area-averaged $\overline{C_P}$ on homogeneous terrain is more conservative than the results on heterogeneous terrain. Therefore, the influence of terrain complexity can be ignored for estimation of the area-averaged $\overline{C_P}$ of the mid-rise building. However, as shown in the case of the area-averaged $\widetilde{C_P}$, terrain complexity causes greater variability in pressure coefficients than in homogeneous terrain, and it can lead to even larger area-averaged $\widetilde{C_P}$ than homogeneous terrains. This would naturally be an effect of wind gustiness. Nevertheless, as shown in Eq. (3), only $\overline{C_P}$ is generally used to estimate the wind load on the building. Therefore, the possible variability of wind load due to the wind gustiness must be further investigated.

This file is the final accepted version of the manuscript, published in https://doi.org/10.1016/j.engstruct.2024.118907

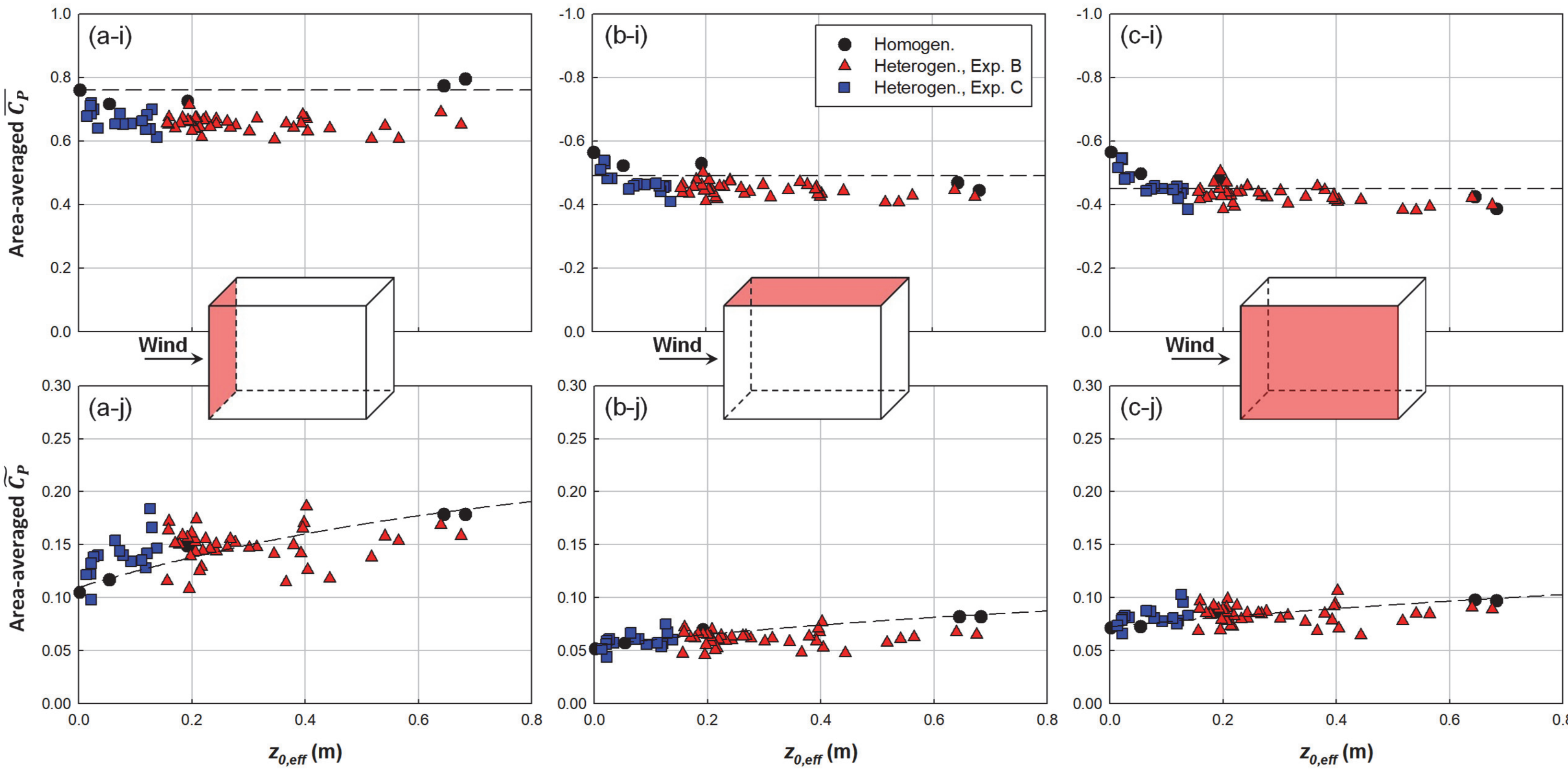

Fig. 12. Comparison of the statistics of area-averaged pressure coefficient over homogeneous and heterogeneous terrains: (a) Windward wall; (b) Roof; and (c) Side wall: with (i) Area-averaged $\overline{C_P}$ and ;(j) Area-averaged $\widetilde{C_P}$.

This file is the final accepted version of the manuscript, published in
https://doi.org/10.1016/j.engstruct.2024.118907

5.3. Gust Effect Factor

The assessment of the gust dynamic pressure factor G_u and gust response factor G_P is crucial for calculating the gust effect factor G, as defined in Eq. (4). Fig. 13 illustrates the impact of (a) $z_{0,\mathrm{eff}}$ and (b) $\mathrm{COV}_{\ln(z_0)}$ on G_u. at the roof height. The black dash in Fig. 13 (a) is the regression result of G_u for homogeneous terrains. G_u demonstrates an increase with the rise of $z_{0,\mathrm{eff}}$, and heterogeneous terrains exhibit larger variability. For instance, at $z_{0,\mathrm{eff}}$ of 0.2 m, G_u on homogeneous terrain is approximately 1.15, while G_u on heterogeneous terrains ranges from 1.10 to 1.27. The influence of terrain complexity can cause an increase of up to 15% in G_u. Complex heterogeneous terrains introduce intricate flow patterns around buildings, contributing to the observed variability in G_u. Fig. 13 (b) elucidates the relationship between $\mathrm{COV}_{\ln(z_0)}$ and G_u. As $\mathrm{COV}_{\ln(z_0)}$ increases, G_u also exhibits a corresponding increase, a trend consistent across both exposures B and C.

Overall, G_u for exposure B and C ranges from 1.08 to 1.27 and 1.10 to 1.22, respectively. This affirmation underscores that, even within the same exposure category, variations of up to 20% can arise due to the changes in $z_{0,\mathrm{eff}}$ and the degree of terrain complexity.

This file is the final accepted version of the manuscript, published in
https://doi.org/10.1016/j.engstruct.2024.118907

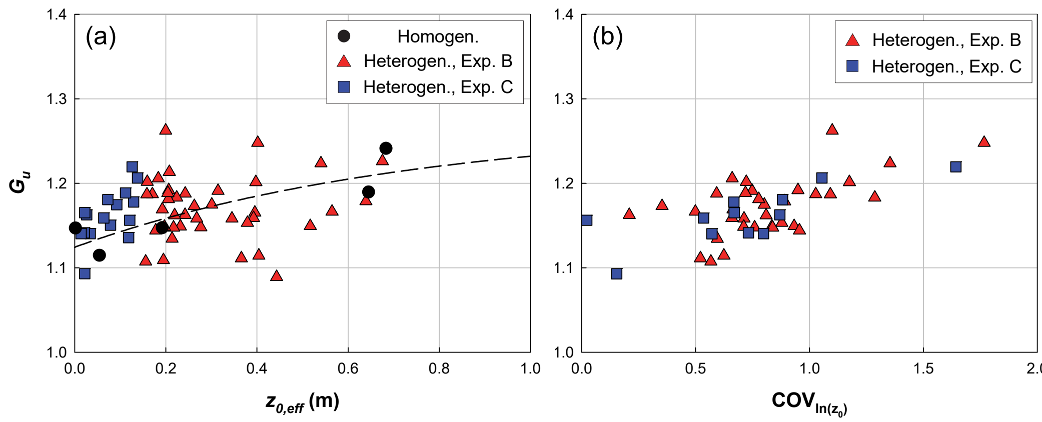

Fig. 13. Gust dynamic pressure factors at roof height: (a) Effect of $z_{0,\mathrm{eff}}$; and (b) Effect of $\mathrm{COV}_{\ln(z_0)}$.

Fig. 14 illustrates the variation in G_P with changing $z_{0,\mathrm{eff}}$ for (a) windward wall, (b) roof, and (c) side wall. Terrain complexity consequently amplifies the variance of G_P. At a $z_{0,\mathrm{eff}}$ of 0.2 m, a G_P of about 1.8 was observed on the windward wall of homogeneous terrain. In contrast, around the same $z_{0,\mathrm{eff}}$ value, a much higher G_P up to 2.2 was observed on heterogeneous terrain, indicating a potential difference of approximately -22 to 17%. Despite both the roof and side wall being flow-separation region, the amplification of G_P on the roof is smaller than that on the side wall. For instance, when $z_{0,\mathrm{eff}}$ was 0.2 m, a G_P of approximately 1.65 was observed on the roof in homogeneous terrain, whereas in heterogeneous terrain, it was amplified to around 1.8. Conversely, on the side wall, a G_P of about 1.85 was observed in the homogeneous terrain, and this amplification reached around 2.13 in the heterogeneous terrain. This difference of amplification may be attributed to the fact that the roof is influenced by wind characteristics at a higher height than the side wall, where turbulence properties are relatively weak. Moreover, G_P is influenced by $\mathrm{COV}_{\ln(z_0)}$, as shown in Fig. 15, where the trend of G_P increasing with higher $\mathrm{COV}_{\ln(z_0)}$ is observed in both exposure B and C.

This file is the final accepted version of the manuscript, published in https://doi.org/10.1016/j.engstruct.2024.118907

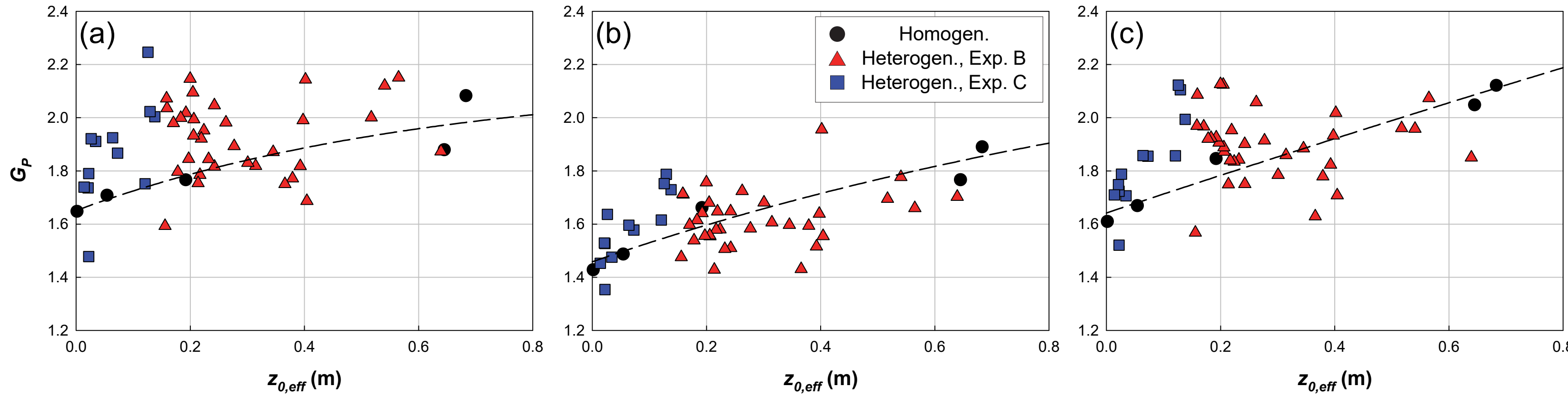

Fig. 14. Gust response factors for varying $z_{0,\mathrm{eff}}$: (a) Windward wall; (b) Roof; and (c) Side wall.

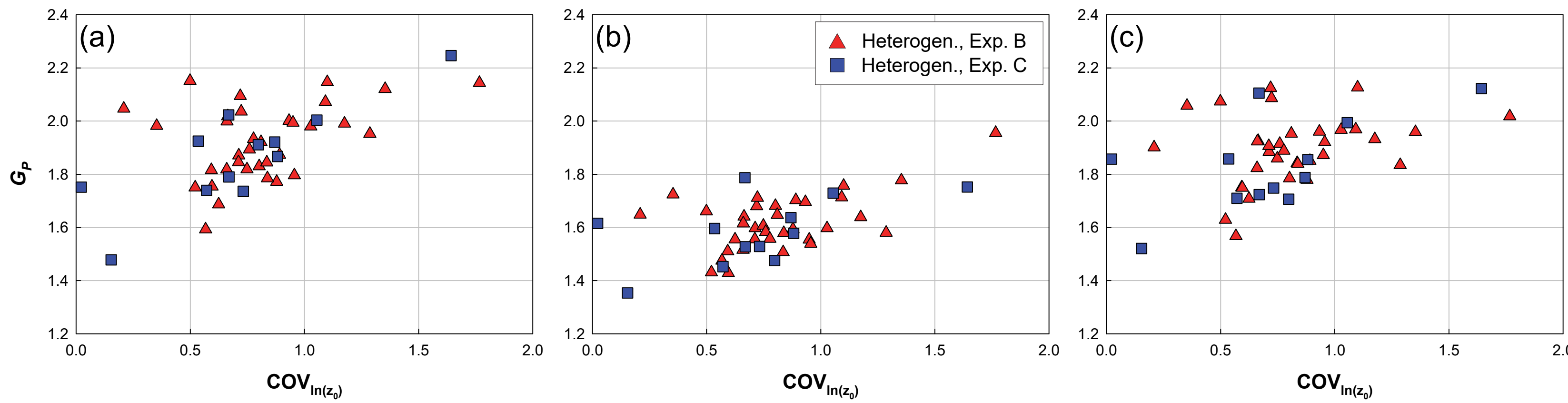

Fig. 15. Gust response factors for varying $\mathrm{COV}_{\ln(z_0)}$: (a) Windward wall; (b) Roof; and (c) Side wall.

This file is the final accepted version of the manuscript, published in
https://doi.org/10.1016/j.engstruct.2024.118907

Figs. 16 and 17 depict the variations in *G* with changing $z_{0,\mathrm{eff}}$ and $\mathrm{COV}_{\ln(z_0)}$, respectively, for (a) windward wall, (b) roof, and (c) side wall. *G* demonstrates no significant change with alterations in $z_{0,\mathrm{eff}}$ and $\mathrm{COV}_{\ln(z_0)}$. Since G_u and G_P increased concurrently with the rise in $z_{0,\mathrm{eff}}$, there is no clear increasing trend in *G*. However, the variability noticeably increased due to terrain complexity. In homogeneous terrain, the average of *G* is approximately 1.33 for windward wall, 1.20 for roof, and 1.36 for side wall. In heterogeneous terrain, it ranges from 1.24 to 1.58 for windward wall, 1.07 to 1.28 for roof, and 1.22 to 1.52 for side wall. Consequently, when comparing *G* on heterogeneous terrain with the average *G* on homogeneous terrain, terrain complexity can increase the *G* of mid-rise building up to -7~19% for windward wall, -10~7% for roof, and -10~12% for side wall.

Identifying the cause of this variation in *G* and precisely estimating the *G* of heterogeneous terrain based on the terrain morphology could significantly enhance the accuracy of predicting wind loads on mid-rise buildings, preventing both underestimation and overestimation. However, as evident in Fig. 17, explaining the cause of such variability in *G* using $\mathrm{COV}_{\ln(z_0)}$ alone was challenging. Unlike G_u and G_P, no clear relationship with $\mathrm{COV}_{\ln(z_0)}$ was observed in *G*. Therefore, further research utilizing higher-dimensional terrain complexity measures, rather than $\mathrm{COV}_{\ln(z_0)}$, must be applied.

This file is the final accepted version of the manuscript, published in https://doi.org/10.1016/j.engstruct.2024.118907

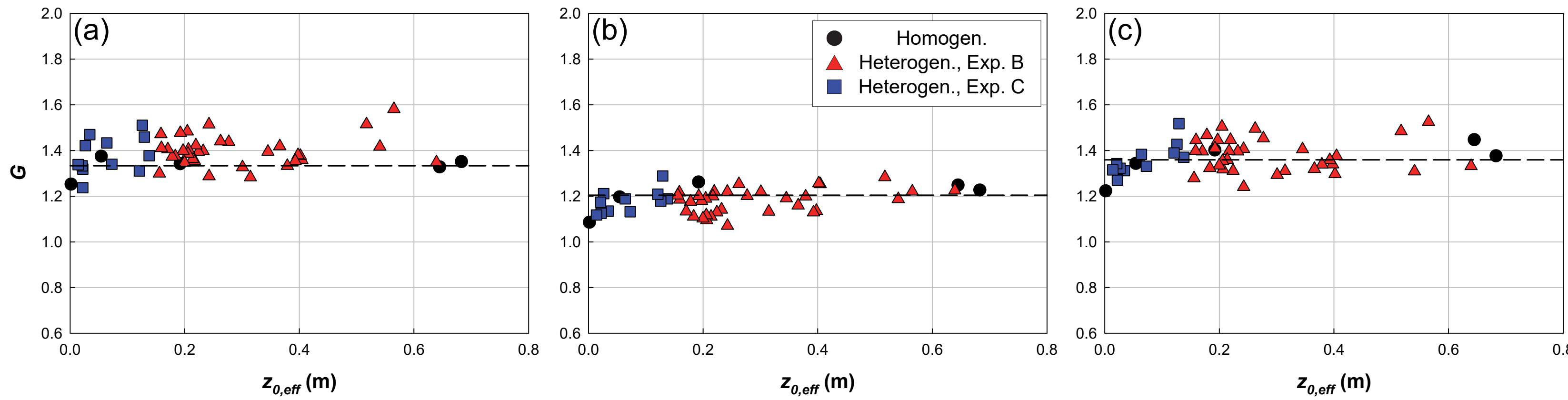

Fig. 16. Gust effect factors for varying $z_{0,eff}$: (a) Windward wall; (b) Roof; and (c) Side wall.

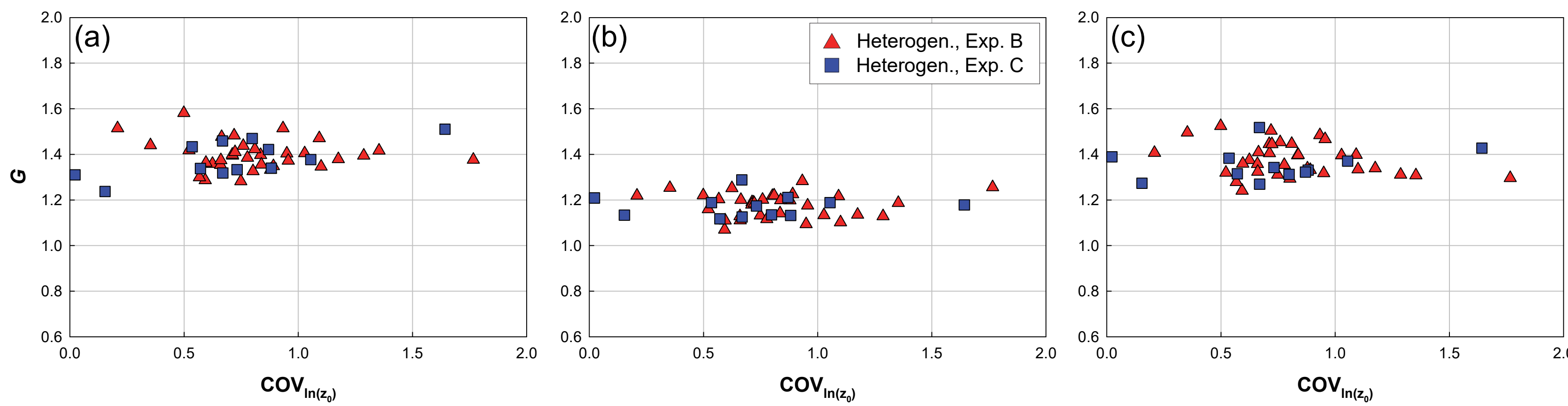

Fig. 17. Gust effect factors for varying $COV_{\ln(z_0)}$: (a) Windward wall; (b) Roof; and (c) Side wall.

This file is the final accepted version of the manuscript, published in
https://doi.org/10.1016/j.engstruct.2024.118907

6. Conclusions

This study conducted extensive wind tunnel tests using 50 actual terrain morphologies in the US to investigate the impact of terrain complexity on the wind pressure of the 50 m-height mid-rise building. The results were compared with testing on homogeneous terrain to analyze variations in wind pressure characteristics and quantify the potential errors that may occur when ignoring terrain complexity. Differences between homogeneous and complex heterogeneous terrains were investigated in the statistics of C_P at tap line, the statistics of area-averaged C_P, and gust effect factor *G*. The nominal values presented in this study are specific to the terrain morphology and building geometry examined and should not be generalized to other contexts. However, the underlying trends provide more significant, broadly applicable insights. The main findings are as follows:

- In investigating the C_P on tap lines, variations in $z_{0,\mathrm{eff}}$ were found to have an insignificant effect on $\overline{C_P}$, while $\widetilde{C_P}$ exhibited an increasing with $z_{0,\mathrm{eff}}$. Moreover, within the same exposure category, the ranges of C_P statistics for homogeneous terrain and complex heterogeneous terrain coincided. For example, the C_P statistics for homogeneous terrain with $z_{0,\mathrm{eff}}$ of 0.7 m, corresponding to the upper bound of exposure B, closely aligned with the upper bound of the results for complex heterogeneous terrain in exposure B.

- The examination of the peak $\overline{C_P}$ and maximum $\widetilde{C_P}$ at the tap lines highlighted that the larger peak $\overline{C_P}$ values were observed in homogeneous terrain compared to complex heterogeneous terrain in windward wall, roof, and side wall due to the lower mean wind speed on complex heterogeneous terrains. The magnitude of peak $\overline{C_P}$ from homogeneous terrain proved to be conservative, with no additional amplification due to terrain complexity. Conversely, it was observed that the magnitude of maximum $\widetilde{C_P}$ could increase by up to 30% in heterogeneous terrain compared to the result from homogeneous terrain, even with similar $z_{0,\text{eff}}$.

- Area-averaged C_P statistics displayed a pattern similar to C_P at tap lines. Area-averaged $\overline{C_P}$ for windward wall, roof, and side wall remained unaffected significantly by changes in $z_{0,\text{eff}}$, while $\widetilde{C_P}$ exhibited an increasing trend with $z_{0,\text{eff}}$. Moreover, it was affirmed that $\overline{C_P}$ in homogeneous terrain closely approached the upper bound of $\overline{C_P}$ in heterogeneous terrain, and that heterogeneous terrain could experience up to a 20% decrease compared to homogeneous terrain. In contrast, for $\widetilde{C_P}$, it was observed that even with $z_{0,\text{eff}}$, it could be amplified by up to 20% in heterogeneous terrain compared to homogeneous terrain. Since $\overline{C_P}$ is the primary statistic considered in wind load design, and its value on homogeneous terrain surpasses that on heterogeneous terrain, it is deemed acceptable to disregard terrain complexity only in $\overline{C_P}$ for this building. However, a comprehensive evaluation of the impact of wind gustiness resulting from terrain complexity necessitates an examination of factors related to wind gustiness.

- Upon investigating G_u calculated using the 3-s average wind speed, a discernible trend emerged that G_u increased with a rise in $z_{0,\text{eff}}$. Furthermore, it was substantiated that even with similar $z_{0,\text{eff}}$, G_u could be amplified by approximately 15% in heterogeneous terrain. Examination of the relationship between $\text{COV}_{\ln(z_0)}$ and G_u revealed that G_u increased as $\text{COV}_{\ln(z_0)}$ increased. That is, an escalation in the degree of terrain complexity led to an amplification of G_u. G_P was also observed to escalate with an increase in $z_{0,\text{eff}}$, with this trend consistently observed for all windward walls, roofs, and side walls. However, on the roof, the amplification of G_P is less pronounced that on the side wall. This difference is attributed to the turbulence property disparity between homogeneous terrain and heterogeneous terrain is less significant on the roof than on the side wall, owing to differences in height.

- Upon investigating G, it was elucidated that G does not exhibit clear trends with $\mathrm{z}_{0,\mathrm{eff}}$ and $\mathrm{COV}_{\ln(\mathrm{z}_0)}$, yet the observed G in heterogeneous terrain displayed considerable variability when compared to the result from homogeneous terrain. As $\mathrm{z}_{0,\mathrm{eff}}$ or $\mathrm{COV}_{\ln(\mathrm{z}_0)}$ increased, G_u and G_P increased simultaneously, contributing to G not responding sensitively to these changes. However, in comparison to G on homogeneous terrain, G for complex heterogeneous terrains could increase by about 19%, 7%, and 12% for windward wall, roof, and side wall, respectively. The impact of terrain complexity on the variability of G was challenging to assess strictly using $\mathrm{COV}_{\ln(\mathrm{z}_0)}$ alone, necessitating higher-dimensional measures. As a result, when evaluating wind load considering the gust effect, if the influence of terrain complexity is ignored, a less conservative design wind load can be calculated.

- To compare the results between the homogeneous terrain and heterogeneous terrain, $\mathrm{z}_{0,\mathrm{eff}}$ values were estimated using a conventional anemometric approach originally developed for homogeneous terrains [48, 49]. Two limitations were observed when the anemometric approach was applied to the complex heterogeneous terrains, which can be investigated in future studies. First, the actual wind speed may differ even if $\mathrm{z}_{0,\mathrm{eff}}$ is calculated similarly between homogeneous and heterogeneous terrains. This is because the anemometric approach fits not only $\mathrm{z}_{0,\mathrm{eff}}$ but also d and u_* together in the log law.

Second, the anemometric approach may slightly underestimate the gradient height δ for the heterogeneous terrains. In the anemometric approach, the upper bound of the fitting range is determined from δ. Thus, such underestimation leads to the same effect as estimating $z_{0,\mathrm{eff}}$ on a smoother terrain. This limitation appears to be inherent in the method of fitting the upper part of the wind profile obtained from a wind tunnel experiment to a quadratic function. These observations suggest that additional boundary conditions or restrictions may be required to apply conventional anemometric approaches to complex heterogeneous terrains. Therefore, the comparison between the homogeneous terrain and heterogeneous terrains in this paper needs careful interpretation until such future studies improve the estimation method of the $z_{0,\mathrm{eff}}$ for heterogeneous terrains.

This file is the final accepted version of the manuscript, published in
https://doi.org/10.1016/j.engstruct.2024.118907

7. Appendix A

Table A 1. $z_{0,\text{eff}}$ in full-scale and corresponding exposure categories for complex heterogeneous terrain.

<table>
<tr><th>Site</th><th>$z_{0,\text{eff}}$ (m)</th><th>Exposure category</th><th>Site</th><th>$z_{0,\text{eff}}$ (m)</th><th>Exposure category</th></tr>
<tr><td>34</td><td>0.014</td><td rowspan="12">C</td><td>17</td><td>0.217</td><td rowspan="21">B</td></tr>
<tr><td>45</td><td>0.021</td><td>10</td><td>0.219</td></tr>
<tr><td>49</td><td>0.022</td><td>5</td><td>0.224</td></tr>
<tr><td>36</td><td>0.022</td><td>2</td><td>0.232</td></tr>
<tr><td>12</td><td>0.026</td><td>41</td><td>0.242</td></tr>
<tr><td>39</td><td>0.034</td><td>42</td><td>0.242</td></tr>
<tr><td>27</td><td>0.064</td><td>19</td><td>0.262</td></tr>
<tr><td>25</td><td>0.073</td><td>15</td><td>0.277</td></tr>
<tr><td>9</td><td>0.121</td><td>38</td><td>0.301</td></tr>
<tr><td>40</td><td>0.126</td><td>47</td><td>0.315</td></tr>
<tr><td>24</td><td>0.129</td><td>46</td><td>0.345</td></tr>
<tr><td>14</td><td>0.138</td><td>1</td><td>0.366</td></tr>
<tr><td>13</td><td>0.156</td><td rowspan="13">B</td><td>35</td><td>0.379</td></tr>
<tr><td>28</td><td>0.158</td><td>23</td><td>0.393</td></tr>
<tr><td>43</td><td>0.159</td><td>21</td><td>0.398</td></tr>
<tr><td>30</td><td>0.171</td><td>18</td><td>0.402</td></tr>
<tr><td>29</td><td>0.178</td><td>26</td><td>0.404</td></tr>
<tr><td>44</td><td>0.183</td><td>20</td><td>0.517</td></tr>
<tr><td>6</td><td>0.192</td><td>11</td><td>0.541</td></tr>
<tr><td>22</td><td>0.197</td><td>37</td><td>0.565</td></tr>
<tr><td>48</td><td>0.200</td><td>31</td><td>0.639</td></tr>
<tr><td>4</td><td>0.205</td><td>33</td><td>0.748</td><td rowspan="4">A</td></tr>
<tr><td>32</td><td>0.206</td><td>7</td><td>0.776</td></tr>
<tr><td>3</td><td>0.206</td><td>8</td><td>0.987</td></tr>
<tr><td>16</td><td>0.214</td><td>50</td><td>1.300</td></tr>
</table>

Table A 2. $z_{0,\text{eff}}$ in full-scale and corresponding exposure categories for homogeneous terrain.

H **(testing scale, m)**	$z_{0,\text{eff}}{}^{*}$ **(m)**	**Exposure category**
0.018	0.002	D
0.028	0.054	C
0.043	0.192	B
0.064	0.645	B
0.077	0.683	B
0.111	1.952	A

*The initially targeted z_0 values were 0.03 m, 0.10 m, 0.30 m, 0.70 m, 1.00 m, and 1.85 m. Based on the Improved Lettau relationship [61], the block height *H* values were inversely determined. Presented $z_{0,\text{eff}}$ values were calculated by the anemometric approach, described in Chapter 3, using the measured wind profile.

This file is the final accepted version of the manuscript, published in
https://doi.org/10.1016/j.engstruct.2024.118907

8. Acknowledgments

This material is based upon work supported by the National Science Foundation under Grant No. CMMI-1856205. Any opinions, findings, and conclusions or recommendations expressed in this material are those of the authors and do not necessarily reflect the views of the National Science Foundation.

9. References

[1] A.G. Davenport, Past, present and future of wind engineering, J. Wind Eng. Ind. Aerodyn. 90(12-15) (2002) 1371-1380. https://doi.org/10.1016/S0167-6105(02)00383-5

[2] ASCE, Minimum design loads and associated criteria for buildings and other structures, 7-22, American Society of Civil Engineers, 2022. https://doi.org/10.1061/9780784415788

[3] K. Wang, T. Stathopoulos, Exposure model for wind loading of buildings, J. Wind Eng. Ind. Aerodyn. 95(9-11) (2007) 1511-1525. https://doi.org/10.1016/j.jweia.2007.02.016

[4] M. Jensen, The model law for phenomena in natural wind, Reprint from Ingenioren (international edition) 2(4) (1958) 121-128.

[5] H.W. Tieleman, Model/full scale comparison of pressures on the roof of the TTU experimental building, J. Wind Eng. Ind. Aerodyn. 65(1-3) (1996) 133-142. https://doi.org/10.1016/S0167-6105(97)00030-5

[6] H. Tieleman, Wind tunnel simulation of wind loading on low-rise structures: a review, J. Wind Eng. Ind. Aerodyn. 91(12-15) (2003) 1627-1649. https://doi.org/10.1016/j.jweia.2003.09.021

[7] C. Grimmond, T.R. Oke, Aerodynamic properties of urban areas derived from analysis of surface form, Journal of Applied Meteorology and Climatology 38(9) (1999) 1262-1292. https://doi.org/10.1175/1520-0450(1999)038%3C1262:APOUAD%3E2.0.CO;2

[8] J. Wiernga, Representative roughness parameters for homogeneous terrain, Boundary-Layer Meteorology 63(4) (1993) 323-363. https://doi.org/10.1007/BF00705357

[9] J. Wang, G.A. Kopp, Comparisons of aerodynamic data with the main wind force–resisting system provisions of ASCE 7-16. I: Low-rise buildings, J. Struct. Eng. 147(3) (2021) 04020347. https://doi.org/10.1061/(ASCE)ST.1943-541X.0002925

[10] J. Wang, G.A. Kopp, Comparisons of Aerodynamic Data with the Main Wind Force–Resisting System Provisions of ASCE 7-16. II: Mid-and High-Rise Buildings, J. Struct. Eng. 147(3) (2021) 04020348. https://doi.org/10.1061/(ASCE)ST.1943-541X.0002922

[11] P. Sachs, Wind forces in engineering, Elsevier2013.

[12] K.H. Kao, Measurements of Pressure-Velocity Correlation on a Rectangular Prism in Turbulent Flow (microfilm), National Library of Canada1970.

[13] R.E. Akins, J.E. Cermak, Wind pressures on buildings, Colorado State University1976.

[14] R.E. Akins, J.A. Peterka, J.E. Cermak, Mean force and moment coefficients for buildings in turbulent boundary layers, J. Wind Eng. Ind. Aerodyn. 2(3) (1977) 195-209. https://doi.org/10.1016/0167-6105(77)90022-8

[15] N. Lin, C. Letchford, Y. Tamura, B. Liang, O. Nakamura, Characteristics of wind forces acting on tall buildings, J. Wind Eng. Ind. Aerodyn. 93(3) (2005) 217-242. https://doi.org/10.1016/j.jweia.2004.12.001
[16] A. Kareem, Measurements of pressure and force fields on building models in simulated atmospheric flows, J. Wind Eng. Ind. Aerodyn. 36 (1990) 589-599. https://doi.org/10.1016/0167-6105(90)90341-9
[17] J. Wang, G.A. Kopp, Gust effect factors for windward walls of rigid buildings with various aspect ratios, J. Wind Eng. Ind. Aerodyn. 212 (2021) 104603. https://doi.org/10.1016/j.jweia.2021.104603
[18] J. Wang, G.A. Kopp, Gust effect factors for regions of separated flow around rigid low-, mid-, and high-rise buildings, J. Wind. Eng. Ind. Aerod. 232 (2023) 105254. https://doi.org/10.1016/j.jweia.2022.105254
[19] J. Yu, M. Li, T. Stathopoulos, Q. Zhou, X. Yu, Urban exposure upstream fetch and its influence on the formulation of wind load provisions, Building and Environment 203 (2021) 108072. https://doi.org/10.1016/j.buildenv.2021.108072
[20] L. An, N. Alinejad, S. Kim, S. Jung, Experimental study on wind characteristics and prediction of mean wind profile over complex heterogeneous terrain, Building and Environment (2023) 110719. https://doi.org/10.1016/j.buildenv.2023.110719
[21] A.F. Akon, G.A. Kopp, Mean pressure distributions and reattachment lengths for roof-separation bubbles on low-rise buildings, J. Wind Eng. Ind. Aerodyn. 155 (2016) 115-125. https://doi.org/10.1016/j.jweia.2016.05.008
[22] M. Kiya, K. Sasaki, Free-stream turbulence effects on a separation bubble, J. Wind Eng. Ind. Aerodyn. 14(1-3) (1983) 375-386. https://doi.org/10.1016/0167-6105(83)90039-9
[23] G. Solari, Gust buffeting. I: Peak wind velocity and equivalent pressure, J. Struct. Eng. 119(2) (1993) 365-382. https://doi.org/10.1061/(ASCE)0733-9445(1993)119:2(365)
[24] G. Solari, Gust buffeting. II: Dynamic alongwind response, J. Struct. Eng. 119(2) (1993) 383-398. https://doi.org/10.1061/(ASCE)0733-9445(1993)119:2(383)
[25] EN, Eurocode 1: Actions on Structures—Part 1–4: General Actions—Wind Actions, EN1994-1-4: 2005, 2005.
[26] D. Banks, R. Meroney, The applicability of quasi-steady theory to pressure statistics beneath roof-top vortices, J. Wind Eng. Ind. Aerodyn. 89(6) (2001) 569-598. https://doi.org/10.1016/S0167-6105(00)00092-1
[27] C.-H. Wu, G.A. Kopp, Examination of the physical assumptions of a quasi-steady vector model using the integral momentum equation, J. Wind. Eng. Ind. Aerod. 187 (2019) 73-84. https://doi.org/10.1016/j.jweia.2019.02.003
[28] Y. Liu, G.A. Kopp, S.-f. Chen, An examination of the gust effect factor for rigid high-rise buildings, Frontiers in Built Environment 6 (2021) 620071. https://doi.org/10.3389/fbuil.2020.620071
[29] N. Alinejad, S. Kim, S. Jung, Wind velocity measurement using heterogeneous terrain representation by Terraformer, in: DesignSafe-CI (Ed.) 2023. https://doi.org/10.17603/ds2-6hg9-r131
[30] N. Alinejad, S. Kim, S. Jung, Wind-Tunnel Testing of Low- and Mid-rise Buildings Under Heterogeneous Upwind Terrains, J. Struct. Eng. (2023).
[31] N. Alinejad, S. Jung, G. Kakareko, P.L. Fernández-Cábán, Wind-Tunnel Reproduction of Nonuniform Terrains Using Local Roughness Zones, Bound. Layer Meteorol. (2023) 1-22. https://doi.org/10.1007/s10546-023-00822-0

[32] F.J. Masters, Boundary Layer Wind Tunnel, Basic Operations Manual, University of Florida, Gainesville, FL, 2017.
[33] R.A. Catarelli, P.L. Fernández-Cabán, B.M. Phillips, J.A. Bridge, F.J. Masters, K.R. Gurley, D.O. Prevatt, Automation and new capabilities in the university of Florida NHERI Boundary Layer Wind Tunnel, Frontiers in Built Environment 6 (2020) 558151. https://doi.org/10.3389/fbuil.2020.558151
[34] R. Kargarmoakhar, A.G. Chowdhury, P.A. Irwin, Reynolds number effects on twin box girder long span bridge aerodynamics, Wind & structures 20(2) (2015) 327-347. https://doi.org/10.12989/WAS.2015.20.2.327
[35] T. Ho, D. Surry, D. Morrish, NIST/TTU cooperative agreement–windstorm mitigation initiative: Wind tunnel experiments on generic low buildings, London, Canada: BLWTSS20–2003, Boundary-Layer Wind Tunnel Laboratory, Univ. of Western Ontario (2003).
[36] Scanivalve, ZOC33 Miniature Pressure Scanner., 2023. http://scanivalve.com/products/pressure-measurement/miniature-analogpressure-scanners/zoc33-miniature-pressure-scanner/. (Accessed April 13rd 2023).
[37] M. Kovaerk, L. Amatucci, K.A. Gillis, F. Potra, J. Ratino, M.L. Levitan, D. Yeo, Calibration of dynamic pressure in a tubing system and optimized design of tube configuration: A numerical and experimental study, in: NIST (Ed.) Technical Note (NIST TN), National Institute of Standards and Technology, Gaithersburg, MD, 2018. https://doi.org/10.6028/NIST.TN.1994
[38] C. Homer, J. Dewitz, L. Yang, S. Jin, P. Danielson, G. Xian, J. Coulston, N. Herold, J. Wickham, K. Megown, Completion of the 2011 National Land Cover Database for the conterminous United States–representing a decade of land cover change information, Photogrammetric Engineering & Remote Sensing 81(5) (2015) 345-354. https://doi.org/10.14358/PERS.81.5.345
[39] A.G. Davenport, Rationale for determining design wind velocities, Journal of the Structural Division 86(5) (1960) 39-68. https://doi.org/10.1061/JSDEAG.0000521
[40] T. Vihma, H. Savijärvi, On the effective roughness length for heterogeneous terrain, Q. J. R. Meteorol. 117(498) (1991) 399-407. https://doi.org/10.1002/qj.49711749808
[41] Y. He, P. Chan, Q. Li, Estimation of roughness length at Hong Kong International Airport via different micrometeorological methods, J. Wind Eng. Ind. Aerodyn. 171 (2017) 121-136. https://doi.org/10.1016/j.jweia.2017.09.019
[42] D. Arthur, S. Vassilvitskii, K-means++ the advantages of careful seeding, Proceedings of the eighteenth annual ACM-SIAM symposium on Discrete algorithms, 2007, pp. 1027-1035.
[43] L.S. Pierre, G. Kopp, D. Surry, T. Ho, The UWO contribution to the NIST aerodynamic database for wind loads on low buildings: Part 2. Comparison of data with wind load provisions, J. Wind Eng. Ind. Aerodyn. 93(1) (2005) 31-59. https://doi.org/10.1016/j.jweia.2004.07.007
[44] J. Lieblein, Efficient methods of extreme-value methodology, Nuclear Energy Agency of the OECD (NEA), Washington, D.C., 1976.
[45] ASCE, Minimum Design Loads and Associated Criteria for Buildings and Other Structures, American Society of Civil Engineers, 2022. https://ascelibrary.org/doi/book/10.1061/9780784415788
[46] NRC, National building code of Canada, Associate Committee on the National Building Code, National Research Council1990.
[47] BS, Eurocode 1: actions on structures–part1-4: general actions-wind actions; BS EN 1991-1-4: 2005, British Standard Institution, London, British Standard, 2005.

[48] A. Karimpour, N. Kaye, Z. Baratian-Ghorghi, Modeling the neutrally stable atmospheric boundary layer for laboratory scale studies of the built environment, Build. Environ. 49 (2012) 203-211. https://doi.org/10.1016/j.buildenv.2011.09.026
[49] R. Catarelli, P. Fernández-Cabán, F. Masters, J. Bridge, K. Gurley, C. Matyas, Automated terrain generation for precise atmospheric boundary layer simulation in the wind tunnel, J. Wind. Eng. Ind. Aerod. 207 (2020) 104276. https://doi.org/10.1016/j.jweia.2020.104276
[50] A.K. Blackadar, H. Tennekes, Asymptotic similarity in neutral barotropic planetary boundary layers, Journal of the Atmospheric Sciences 25(6) (1968) 1015-1020. https://doi.org/10.1175/1520-0469(1968)025%3C1015:ASINBP%3E2.0.CO;2
[51] N.J. Cook, Designers guide to wind loading of building structures. Part 1, US, 1986.
[52] H. Schlichting, K. Gersten, Boundary-layer theory, springer2016.
[53] Y. Uematsu, N. Isyumov, Wind pressures acting on low-rise buildings, J. Wind Eng. Ind. Aerodyn. 82(1-3) (1999) 1-25. https://doi.org/10.1016/S0167-6105(99)00036-7
[54] R. Macdonald, Modelling the mean velocity profile in the urban canopy layer, Boundary-Layer Meteorology 97 (2000) 25-45. https://doi.org/10.1023/A:1002785830512
[55] J. Guo, Turbulent velocity profiles in clear water and sediment-laden flows, Colorado State University1998.
[56] ESDU, Data item 82026. Strong winds in the atmospheric boundary layer. Part 1: hourly-mean wind speeds., Engineering Sciences Data Unit, London, 1993.
[57] ESDU, Data item 85020. Characteristics of atmospheric turbulence near the ground. Part II: single point data for strong winds (neutral atmospheric), Engineering Sciences Data Unit, London, 1985.
[58] P. Welch, The use of fast Fourier transform for the estimation of power spectra: a method based on time averaging over short, modified periodograms, IEEE Transactions on audio and electroacoustics 15(2) (1967) 70-73. 10.1109/TAU.1967.1161901
[59] ESDU, Characteristics of atmospheric turbulence near the ground, Part I: Definitions and general information, Engineering Sciences Data Unit 74030 (1974).
[60] C.-H. Wu, G.A. Kopp, A quasi-steady model to account for the effects of upstream turbulence characteristics on pressure fluctuations on a low-rise building, J. Wind Eng. Ind. Aerodyn. 179 (2018) 338-357. https://doi.org/10.1016/j.jweia.2018.06.014
[61] R. Macdonald, R. Griffiths, D. Hall, An improved method for the estimation of surface roughness of obstacle arrays, Atmospheric environment 32(11) (1998) 1857-1864. https://doi.org/10.1016/S1352-2310(97)00403-2